

Bifunctional α -MnO₂ and Co₃O₄ Catalyst for Oxygen Electrocatalysis in Alkaline Solution

Michael F. Fink,^{*[a, c]} Julia Eckhardt,^[a] Prashant Khadke,^[a] Thorsten Gerdes,^[b, c] and Christina Roth^[a, c]

This work is dedicated to Prof. Monika Willert-Porada. We kindly would like to thank her for her contribution to the project and her support.

Low cost and abundant catalysts demonstrating high activity and stability towards the oxygen reactions, i.e., the oxygen reduction (ORR) and oxygen evolution reaction (OER), are crucial for the development of electrically rechargeable zinc-air batteries. Herein, the facile synthesis and systematic characterisation of two highly active and stable oxygen electrocatalysts, i.e., high surface area α -MnO₂ microspheres and nanoparticulate Co₃O₄, are reported. α -MnO₂ exhibits low half-wave potential and potential of -0.197 and -0.226 V (vs. Ag/AgCl) at -3 mA cm⁻², respectively, that are only marginally higher compared to commercial Pt/C ($E_{1/2} = -0.161$ V, $E_{j=3} = -0.171$ V) for ORR. Meanwhile, Co₃O₄ needs a potential of 0.601 V (vs. Ag/

AgCl) to drive 10 mA cm⁻² being competitive to commercial Ir/C ($E_{j=10} = 0.60$ V) for OER. In order to create a bifunctional catalyst, two approaches were pursued: i) Co₃O₄ nanoparticles were homogeneously grown on the surface of α -MnO₂ microspheres yielding a radial hybrid composite catalyst material in the form of a core (α -MnO₂) shell (Co₃O₄) structure and ii), much simpler, individual α -MnO₂ microspheres and Co₃O₄ nanoparticles were physically mixed in a powder blend. The powder blend demonstrates superior overall bifunctional catalytic properties such that the individual catalysts still dominate their respective oxygen reaction and, due to synergistic interactions between both catalysts, an improved ORR activity could be achieved.

1. Introduction


A modern technological society without batteries has become unthinkable. The rapidly growing use of portable electronic devices, increasing electrification of road transportation and storage of renewable electricity, particularly from intermittent sources such as wind and solar radiation, make reliable and economical battery technologies more important than ever. Currently lithium-ion batteries (LIB) are still the battery of choice for these fields of application, although they are already reaching their performance limits (< 350 Wh kg⁻¹), as well as suffer from additional problems such as potential safety issues, detrimental environmental impacts and relatively high costs, thus making it crucial to promote alternative battery technolo-


gies, so-called post LIB, being capable of meeting upcoming energy storage demands not only in terms of higher energy density but also in operational safety, cost effectiveness and environmental and climatic benignity. Secondary (i.e., electrically rechargeable) zinc-air batteries (ZAB), a well-known representative of the class of aqueous metal-air batteries (MAB), are considered a very promising post LIB technology.^[1,2] ZAB roughly consist of a metallic zinc anode, alkaline electrolyte (i.e. concentrated aqueous potassium hydroxide (KOH)) and a porous air/O₂ breathing cathode utilizing O₂ from ambient air as the positive active material and thus enabling higher energy density (1353 Wh kg⁻¹) compared to LIB and other battery types.^[3] In addition to that, ZAB hold sufficient material availability (Zn is the 24th most abundant element in Earth's crust and can be fully recycled), low cost ($< \$100$ kW⁻¹ h⁻¹), inherent safety (metallic Zn has very low reactivity and can be handled in humid air) and environmental friendliness as well as stand out from other MAB in terms of better corrosion stability in aqueous electrolyte, low self-discharge, long shelf life and a reasonably high theoretical working voltage.^[1,4] While primary (i.e. not rechargeable) ZAB is a mature technology well established in consumer products such as hearing aids, their use as secondary batteries, however, has so far been impeded due to challenges associated with the reversibility of the zinc-anode as well as the air-cathode. Air-cathodes, so-called gas diffusion electrodes (GDE), for secondary ZAB require electrocatalysts demonstrating high (bifunctional) activity and (electro-)chemical stability to efficiently enable both the discharge and charge reaction, i.e. the oxygen reduction reaction (ORR) and oxygen evolution reaction (OER), respectively.^[5-7] Although precious metal catalysts, i.e. carbon supported nanoscale Pt, Ru,

[a] M. F. Fink, J. Eckhardt, Dr. P. Khadke, Prof. C. Roth
Chair of Electrochemical Process Engineering
University of Bayreuth
Universitätsstraße 30, 95447 Bayreuth, Germany
E-mail: michael.fink@uni-bayreuth.de

[b] Prof. T. Gerdes
Chair of Ceramic Materials Engineering
Keylab Glass Technology
University of Bayreuth
Prof.-Rüdiger-Bormann-Str. 1, 95447 Bayreuth, Germany

[c] M. F. Fink, Prof. T. Gerdes, Prof. C. Roth
Bavarian Center for Battery Technology (BayBatt)
University of Bayreuth
95447 Bayreuth, Germany

 Supporting information for this article is available on the WWW under <https://doi.org/10.1002/celec.202001325>

 © 2020 The Authors. ChemElectroChem published by Wiley-VCH GmbH. This is an open access article under the terms of the Creative Commons Attribution License, which permits use, distribution and reproduction in any medium, provided the original work is properly cited.

Ir, or alloys thereof, are considered state of the art, viz., to offer the highest ORR and OER catalytic activity, their scarcity, high costs and poor stability in alkaline electrolyte limits their applicability in electrically rechargeable ZAB.^[8,9] This has given rise to extensive research and development in the past decade focusing on lower cost alternatives along with strategies to improve the catalytic activity and electrochemical stability of the like. A great wealth of literature towards potentially suitable bifunctional non-precious metal catalyst materials for secondary ZAB cataloging catalyst performance and durability parameters as well as their relationship to various physicochemical and structural properties, sometimes even outperforming the ORR and OER properties of its precious metal counterparts, are available and have already been summarized and evaluated in previous reviews.^[3,7,10–12] Among them transition metal oxides (TMOs) or composite materials comprised of mixed TMOs, while one holding superior electrocatalytic activity for the ORR and the other one for the OER, are of great interest as catalysts for electrically rechargeable ZAB.^[13] Especially the combination of manganese oxides (MnO_2) and cobalt oxides (Co_3O_4) is promising to be used as a composite catalyst material.^[8,14,15] Compared to precious metal based catalysts, MnO_2 and Co_3O_4 are inexpensive and readily available along with superb catalytic activity and electrochemical stability in alkaline electrolyte.^[15] Especially MnO_2 , which can occur in various polymorphs depending on its crystallographic structure, Mn oxidation state and Mn/O stoichiometry within the compound, has gained significant interest and is still the focus of research and development as alternative to precious metal based catalysts.^[16] To date, the electrocatalytic activity of MnO_2 for the ORR^[17–20] and OER^[3,9,21–23] has already been proven. More important, Meng and co-workers prepared an array of MnO_2 catalyst materials by utilizing various synthesis routes and studied the effect of crystallographic structure for catalysing ORR and OER.^[22] They found, that the tunnel-type α crystallographic structure of MnO_2 (α - MnO_2) yields the highest bifunctional performance and demonstrates a potential difference, ΔE , i.e., the difference between a potential at -3 mA cm^{-2} ($E_{j=3}$) and 10 mA cm^{-2} ($E_{j=10}$) for ORR and OER, respectively, of mere 0.96 V as well as reasonable OER durability ($> 3 \text{ h}$) during chronopotentiometric stability tests at a constant current density of 5 mA cm^{-2} . Zheng and co-workers synthesized 3d radially hierarchical α - MnO_2 catalyst materials via a hydrothermal route and the dandelion-like morphology represents a ΔE of 1.05 V as well as a current retention of 85% after 10 h of constant potential chronoamperometric operation at -0.5 V (vs. Ag/AgCl) during ORR.^[23] Selvakumar and co-workers studied the shape-dependent bifunctional activity of α - MnO_2 and measured the highest ORR and OER activity for a nano-wire like morphology synthesized via a hydrothermal route.^[9,24] Furthermore, several other material characteristics, i.e., exposure of certain dominant crystallographic facets^[8,9], the amount of surface (physically bound) and structural (chemically bound) water^[8] as well as cation ($\text{Mn}^{4+}/\text{Mn}^{3+}$) and oxygen vacancy defects^[8,25–28], which are considered to appear as or give rise to ORR and OER catalytically active sites within α - MnO_2 -based materials, were studied experimentally as well as theoretically and correlated with their intrinsic

electrocatalytic activity. Apart from the above mentioned material characteristics, the specific surface area remains one of the most relevant material properties since it triggers the exposure of certain catalytically active sites.^[29] Even though α - MnO_2 alone demonstrates sufficient bifunctional activity, its OER performance requires improvement. One possible strategy to enhance the OER activity and therefore bifunctional performance is the construction of a composite catalyst by combining two individual catalysts, while one demonstrates high ORR and the other one high OER activity, and thus integrating their individual ORR and OER active sites into the composite material.^[30] Meanwhile, Co_3O_4 has also been studied as a superior catalyst towards OER and, consequently, makes it a suitable partner for constructing a bifunctional composite catalyst together with α - MnO_2 .^[31–40]

The aim of this work is the development of a composite catalyst material containing α - MnO_2 and Co_3O_4 for electrically rechargeable ZAB possessing high catalytic activity and stability in aqueous KOH electrolyte. In order to tailor a bifunctional catalyst, two approaches were pursued: i) Co_3O_4 nanoparticles were homogeneously grown on the surface of α - MnO_2 to yield a radial hybrid composite material in the form of a core (α - MnO_2) shell (Co_3O_4) structure and ii), much simpler, individual α - MnO_2 microspheres and Co_3O_4 nanoparticles were physically mixed in a powder-blend. Electrocatalytic activity and stability with respect to the ORR and OER in alkaline electrolyte of the as-synthesized individual catalysts and composite catalyst materials were investigated using the Thin-Film Rotating Disk Electrode (TF-RDE) technique. Structural and physicochemical properties relevant for catalysis were examined by powder X-ray diffraction (PXRD), Scanning electron microscopy (SEM), Energy dispersive X-ray spectroscopy (EDS), Inductively coupled plasma optical emission spectrometry (ICP-OES) and nitrogen adsorption-desorption.

2. Results and Discussion

2.1. Physicochemical and Structural Characterisation

2.1.1. α - MnO_2 Microspheres

Figure 1a, 1c and 1d show SEM images of the α - MnO_2 catalyst at different magnifications. As-synthesized α - MnO_2 catalyst secondary particles can be best described as isolated highly uniform spheres with an average diameter of $2.5 \mu\text{m}$ (average size of secondary particles based on evaluation of 1000 microspheres) (Figure 1b). Higher magnification reveals α - MnO_2 microspheres as 3D-hierarchically structured aggregates of cross-linked arbitrarily oriented needles (primary particle shape) with a diameter, D , and length, L , in the range of 10 nm and 30 nm, respectively (Figure 1d and 1e). Both ICP-OES and EDS indicate the presence of K, Ag and Mn. Based on EDS spectra recorded on a dense α - MnO_2 microspheres powder sample an elemental composition of 0.91 at.-% K, 0.54 at.-% Ag, 37.21 at.-% Mn and 61.36 at.-% O can be calculated (Figure S1). While Mn and O can be certainly related to MnO_2 ($\text{Mn}:\text{O} \approx 1:2$), K and Ag

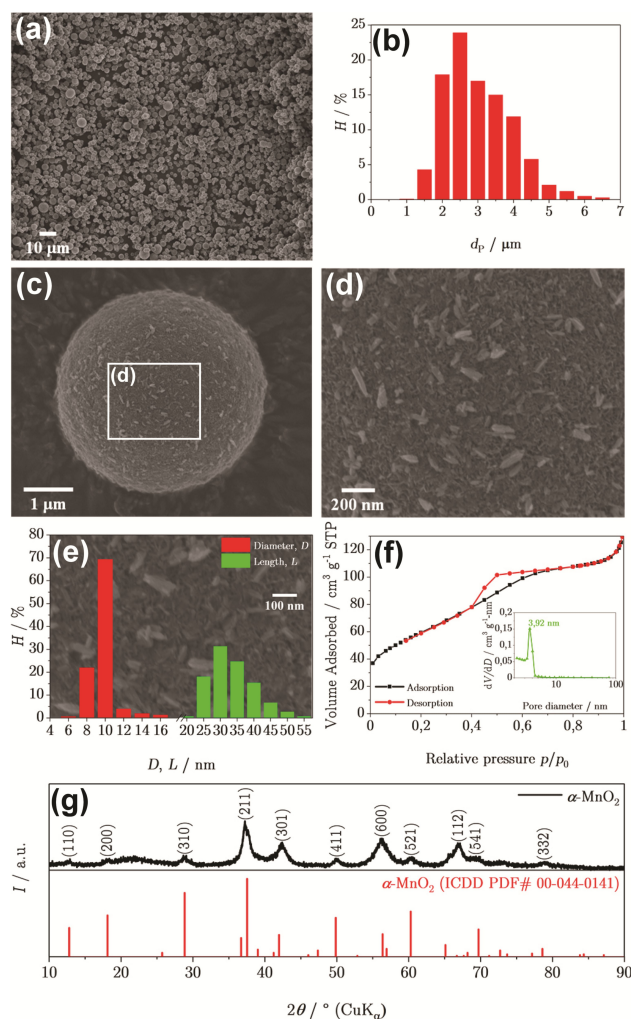


Figure 1. a) SEM image of α -MnO₂ microspheres, b) distribution of α -MnO₂ microspheres secondary particle size based on evaluation of 1000 microspheres, c) SEM image of a single α -MnO₂ microsphere, d) higher magnification SEM image showing the agglomerated needle-like primary particles, e) distribution of diameter, D , and length, L , of the needle-like primary particles based on evaluation of 150 needles, f) N₂ adsorption-desorption isotherms and BJH pore size distribution (inset), g) PXRD reflection pattern of as-synthesized α -MnO₂ microspheres.

could be trace contaminants from the synthesis that have not been completely removed during washing. In contrast to EDS, ICP-OES (not included) detected an Ag content up to 13.65 wt.-% relative to the total metal (K, Ag, Mn) content. This is due to the limiting penetration depth of EDS within the huge microspheres structure that allows only probing the near-surface elemental composition, whereas ICP-OES probes the entire material providing the true bulk composition of the sample. However, taking into account both the EDS and ICP-OES results, it appears that Ag is not homogeneously distributed, but rather we assume an increasing Ag concentration gradient towards the nucleus of the microspheres. Structural characteristics of the as-synthesized α -MnO₂ microspheres have been studied by means of powder X-Ray Diffraction (PXRD). In general, the experimental PXRD reflection pattern of an α -MnO₂ powder sample in Figure 1g shows significantly broadened and low

intensity weak reflections (low crystallinity) indicating small crystallite size as well as the presence of lattice defects. Though a slight shift to lower 2θ angles can be noticed, the reflections observed at angles 2θ 28.93°, 37.23°, 42.41°, 49.95°, 56.29°, 60.35°, 66.97° as well as weak reflections at 12.79°, 18.13°, 69.75° and 78.93° can be well indexed to the (310), (211), (301), (411), (600), (521), (112), (110), (200), (541) and (332) crystallographic planes of tetragonal α -MnO₂ (ICDD PDF No. 00-044-0141, space group I4/m, $a = b = 9.7847$ Å, $c = 2.8630$ Å).

Since no diffraction peaks of designated Ag and K compounds can be identified, the left shift of reflections could be due to doping of Ag and K into α -MnO₂. Doping can either take place by substituting respective manganese ions in the Mn-O framework, or by occupying 2×2 tunnels, both being mainly dependent on the crystal radii of the dopants as well as their coordination.^[41,42] To further investigate a possible bi-doping of Ag and K, interplanar spacing (d -spacing) and lattice parameter were calculated from the angular positions of the diffraction peaks using Bragg's law. D -spacing was determined consulting the most intense reflection of (211) crystallographic plane. In comparison to the corresponding 2.395 Å d -spacing of (211) crystallographic plane at 37.532° 2θ in pristine α -MnO₂ (ICDD PDF No. 00-044-0141), an increased d -spacing of 2.4039 Å can be calculated for the as-synthesized α -MnO₂ microspheres using the shifted (211) reflection at about $2\theta = 37.3784^\circ$. Calculation of lattice parameter was performed by consulting the (600) and (211) crystallographic plane. As did the d -spacing, the lattice parameters and therefore unit cell size ($a = b = 9.7981$ Å, $c = 2.8911$ Å) have also increased compared to pure α -MnO₂. At this point, the question arises as to how K and Ag are integrated into α -MnO₂. As discussed above, there are two possible configurations of K,Ag doped α -MnO₂: i) K,Ag-substituted and ii) K,Ag-interstitial α -MnO₂.^[41,42] A good overview about α -MnO₂ materials doped with various metal ions as well as their structural and electrochemical properties relevant for energy storage and conversion is provided by Julien and co-workers.^[43] Generally, α -MnO₂ is built of double chains of MnO₆ octahedra arranged at its edges and corners in a square 2×2 fashion to form tunnels, the side length of which is 4.6 Å.^[44–47] It has been widely accepted that relatively large ions or such with similar radii to the dimensions of the tunnels as well as allowing eight-coordination, respectively, favour to settle within this tunnels.^[48] Among them, K⁺-interstitial α -MnO₂ (K_xMn₈O₁₆), so-called cryptomelane type α -MnO₂, has already been successfully synthesized and investigated in great detail.^[21,49] In contrast, smaller ions allowing six-coordination and with similar radii (also referred to as Shannon-Prewitt crystal radius) to ^{VI}Mn⁴⁺ (0.67 Å) or ^{VI}Mn³⁺ (0.72 Å at low spin, 0.785 Å at high spin), respectively, are preferably incorporated into the crystal framework.^[42,50] In the light of this, it can be claimed that K⁺ (1.65 Å in eight-coordination) is preferentially introduced into the 2×2 tunnels. However, since the crystal radius of ^{VI}Ag⁺ (1.29 Å) is more than twice that of ^{VI}Mn⁴⁺ or ^{VI}Mn³⁺, respectively, it cannot be completely ruled out that Ag ions (1.42 Å in eight-coordination) do not also occupy the tunnels. While many studies on Ag⁺-interstitial α -MnO₂ are available in literature^[51–53], Ag⁺-substituted α -MnO₂ has not been reported

in the literature, at least to our knowledge. On the other hand, for Ag^+ , framework substitution is more likely to appear than for the much larger K^+ ions.^[42] Or even a competing mechanism occurs, whereby the tunnels are initially occupied by K^+ until complete depletion, subsequently Ag^+ is introduced and remaining Ag^+ is finally incorporated into the crystal framework substituting manganese ions, both being responsible for the left shift of reflections in the PXRD reflection pattern as well as increased d -spacing and lattice parameters. Besides the distortion of the crystalline structure that can promote the formation of material properties relevant for catalysis, the introduction of K^+ and Ag^+ into the tunnel structure as well as substitution of manganese with lower valence Ag^+ can alter the Mn oxidation state, viz., from Mn^{4+} to Mn^{3+} , being crucial for manifesting manganese cation defects and oxygen vacancies, respectively, which are considered to be the catalytically active sites of α - MnO_2 materials.^[24,54]

N_2 adsorption-desorption isotherms and Barrett-Joyner-Halenda (BJH) pore size distribution curves of an α - MnO_2 powder sample are presented in Figure 1f. α - MnO_2 microspheres exhibit a typical type IV isotherm accompanied with a H2(a) hysteresis loop in a $0.4 < p/p_0 < 0.7$ range according to IUPAC classification.^[55] The observed shape of the hysteresis loop is characteristic for mesoporous materials possessing a complex ordered network structure, that is likewise already indicated by the higher magnification SEM images of single α - MnO_2 microspheres. The BJH pore size distribution curve derived from the desorption branch features a narrow maximum in the ~ 3 to ~ 4.5 nm mesoporous range (3.9 nm BJH average pore diameter) suggesting homogenous pore diameters as well as high uniformity mesopores.^[55,56] Furthermore α - MnO_2 displays high BJH cumulative pore volume and BET specific surface area of $0.223 \text{ cm}^3 \text{ g}^{-1}$ and $214.6 \text{ m}^2 \text{ g}^{-1}$, respectively, the latter being the highest BET specific surface area for an α - MnO_2 with reasonably distinct crystallinity ever reported so far.^[22,57–71]

2.1.2. Nanoparticulate Co_3O_4

As can be seen in Figure 2a and 2b, as-synthesized Co_3O_4 catalyst is composed of spherical particles forming loosely-stacked porous agglomerates. Figure 2c represents the particle size distribution of Co_3O_4 nanoparticles, and the average diameter, d , was determined to be around 30 nm (average size of primary particles based on evaluation of 250 particles). Unlike α - MnO_2 , the PXRD reflection pattern of the Co_3O_4 catalyst powder sample in Figure 2e shows narrow and sharp reflections indicating significantly larger crystallites and a higher degree of crystallinity.

PXRD reflections observed at 19.14° , 31.39° , 36.97° , 38.81° , 44.96° , 55.77° , 59.52° and 65.33° 2θ can be well assigned to the (111), (220), (311), (222), (400), (422), (511) and (440) crystallographic planes of cubic Co_3O_4 (ICDD PDF No. 00-016-4508, space group $\text{Fd-}3\text{m}$).^[72] As no characteristic reflections of impurities or other phases as well as obvious shift of reflections

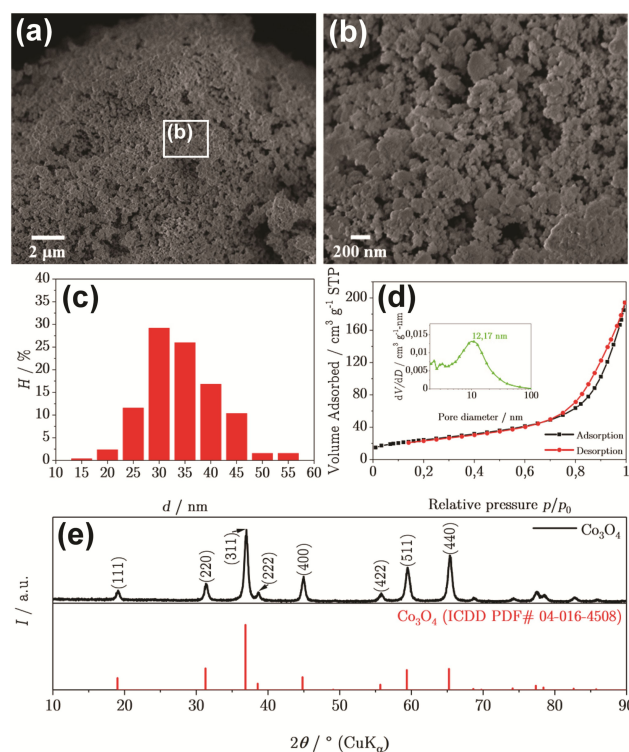


Figure 2. a) SEM image of a Co_3O_4 nanoparticle agglomerate, b) higher magnification SEM image, c) size distribution of Co_3O_4 nanoparticles based on evaluation of 250 nanoparticles, d) N_2 adsorption-desorption isotherms and BJH pore size distribution (inset), e) PXRD reflection pattern of as-synthesized Co_3O_4 nanoparticles.

could be observed, the synthesis routes and conditions can be considered to yield high-purity Co_3O_4 .

Based on EDS spectra recorded on a dense Co_3O_4 nanoparticles powder sample, an elemental composition of 65.3 at-%Co and 34.6 at-%O can be calculated (Figure S2), that matches quite well with the stoichiometry of Co_3O_4 (Co:O \approx 3:4). No other impurities could be found, which is also in good agreement with ICP-OES measurements (not included).

N_2 adsorption-desorption isotherms and the BJH pore size distribution curve of a Co_3O_4 powder sample are presented in Figure 2d. In the case of Co_3O_4 nanoparticles mesoporous and macroporous features could be revealed by the N_2 adsorption-desorption isotherms, for such isotherms are categorized as typical type IV isotherm with a H3-type hysteresis loop in a $0.7 < p/p_0 < 1$ range according to IUPAC classification.^[55] Since capillary condensation occurs at a high relative pressure $p/p_0 \approx 1$ mesopores with large diameters must be present, that is also confirmed by the broad pore size distribution curve calculated by the BJH method from the desorption branch of the N_2 adsorption-desorption isotherms. Pore size distributions range from ~ 4 to ~ 65 nm (12.2 nm BJH average pore diameter) and are mainly originating from the piled up porosity of aggregated mesoporous Co_3O_4 nanoparticles, which was also observed for nanoparticulate Co_3O_4 in a recent study.^[73] BET specific surface area of the Co_3O_4 nanoparticles was evaluated to be $87.6 \text{ m}^2 \text{ g}^{-1}$, which is in the range of previously reported

Co₃O₄ based catalysts.^[31,74–79] BJH cumulative pore volume was determined to be 0.303 cm³ g⁻¹.

High specific surface area and pore volume of α -MnO₂ microspheres and Co₃O₄ nanoparticles significantly enlarge the accessible electrochemical surface area providing abundant exposed catalytically active sites, thereby enhancing the overall ORR and OER performance of the catalysts. Furthermore, the ordered hierarchical network of homogeneous and highly uniform mesopores within α -MnO₂ microspheres can notably promote mass-transfer of reactants and products as well as shorten diffusion pathways for electrons and ions during ORR. Additionally the broad pore size distribution including larger (meso-)pores of Co₃O₄ nanoparticles can in particular facilitate removal of O₂ formed during OER and therefore prevent O₂ bubbles blocking active sites and thereby reaction interface.^[29,80]

2.2. Electrochemical Characterisation

2.2.1. ORR Activity and Stability Evaluation

Cyclic Voltammograms (CVs) of thin-films of the catalysts were collected on a RDE three-electrode configuration at 1600 rpm to evaluate the ORR catalytic kinetic activity. The cathodic sweep of the 2nd CV of the α -MnO₂ microspheres, Co₃O₄ nanoparticles and the commercial 20 wt.-% Pt@XC-72 and 20 wt.-% Ir@XC-72 catalyst are presented in Figure 3a. α -MnO₂ microspheres exhibit a low half-wave potential of -0.197 V (vs. Ag/AgCl (sat. KCl)), which is only marginally higher than that of the commercial 20 wt.-% Pt@XC-72 catalyst ($E_{1/2} = -0.161$ V). In contrast, the ORR on Co₃O₄ nanoparticles and 20 wt.-% Ir@XC-72 begins at more negative potentials, which is why they display significantly higher half-wave potentials of -0.647 V (vs. Ag/AgCl (sat. KCl)) and -0.331 V (vs. Ag/AgCl (sat. KCl)),

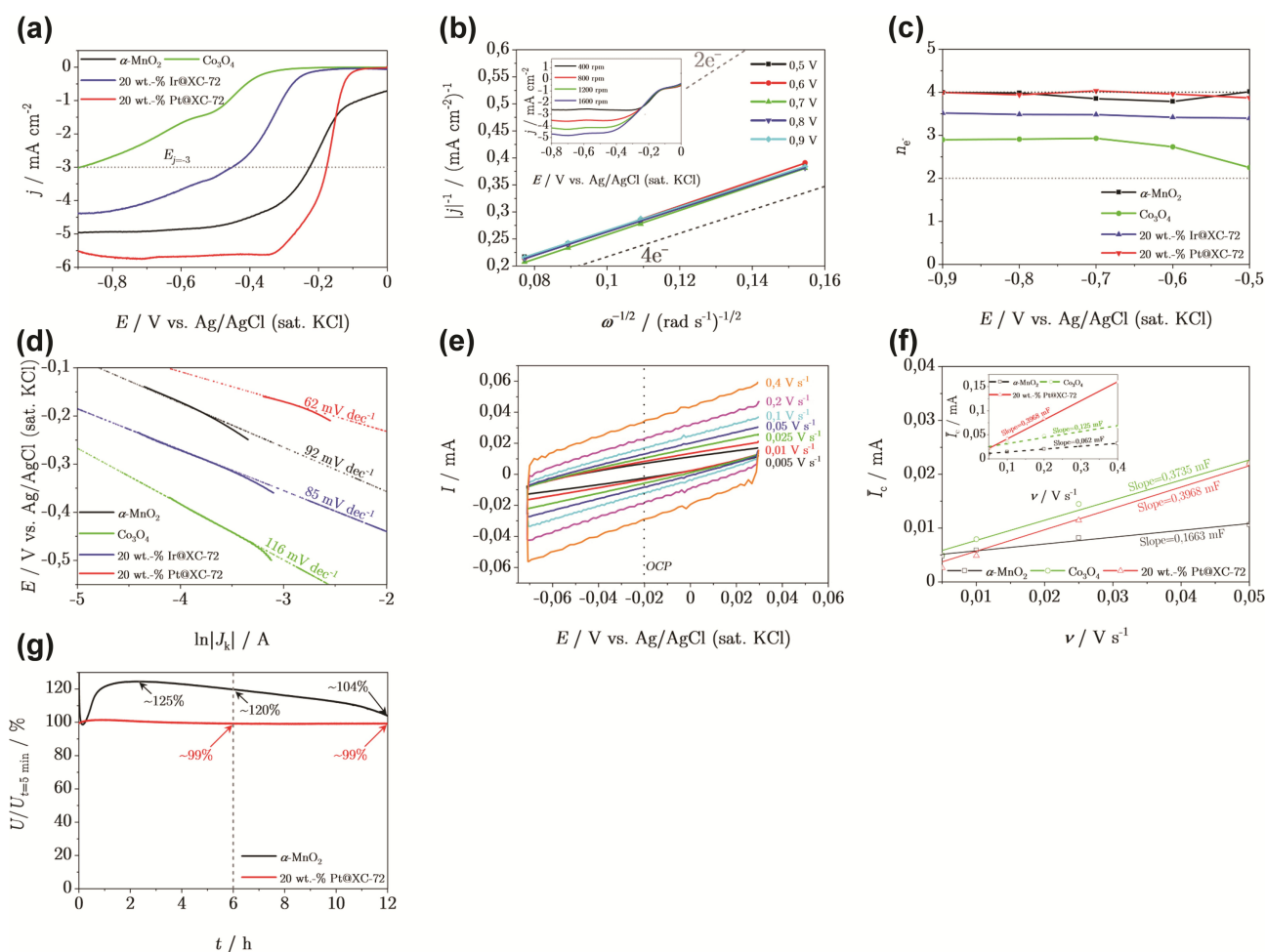


Figure 3. ORR performance and stability evaluation. a) *iR*- and *bg*-corrected LSV curves of α -MnO₂ microspheres, Co₃O₄ nanoparticles, 20 wt.-% Ir@XC-72 and 20 wt.-% Pt@XC-72 in 25 °C equilibrated O₂-saturated 0.1 M KOH at a potential scan-rate of 10 mV s⁻¹ and rotational speed of 1600 rpm within the ORR, b) K-L plots of α -MnO₂ microspheres obtained at different potentials from the *iR*- and *bg*-corrected LSV curves at various rotational speeds performed in 25 °C equilibrated O₂-saturated 0.1 M KOH at a potential scan-rate of 10 mV s⁻¹ (inset), c) number of electrons transferred calculated from the K-L plots of the catalysts within a potential window of -0.5 to -0.9 V (vs. Ag/AgCl (sat. KCl)), d) Tafel plots (dashed lines) to the linear portion of the LSV curves in the low current region of the catalysts (solid lines), e) CVs of α -MnO₂ microspheres obtained in 25 °C equilibrated N₂-saturated 0.1 M KOH at various potential scan-rates in the non-Faradaic potential region, f) average of anodic and cathodic capacitive charging currents measured in the OCP of catalysts as a function of the potential scan-rate, g) *iR*-corrected ORR constant current chronopotentiometric response of α -MnO₂ microspheres and 20 wt.-% Pt@XC-72 in 25 °C equilibrated O₂-saturated 0.1 M KOH at a rotational speed of 1600 rpm and constant current density operation of -3 mA cm⁻².

respectively. The potential at -3 mA cm^{-2} , $E_{j=-3}$, that may represent the more practical comparative value^[81], follows a trend similar to that observed for $E_{1/2}$, although $E_{j=-3}$ turns out higher, particularly in the case of 20 wt.-% Ir@XC-72 and Co_3O_4 . From Figure 3a $E_{j=-3}$ was determined to be -0.226 , -0.177 , -0.894 and -0.452 V (vs. Ag/AgCl (sat. KCl)) for $\alpha\text{-MnO}_2$ microspheres, 20 wt.-% Pt@XC-72, Co_3O_4 nanoparticles and 20 wt.-% Ir@XC-72, respectively. Furthermore, diffusion limiting current densities, j_L , and kinetic current densities, j_k , of the catalysts are calculated. The diffusion limiting current density is determined as an average of the measured current density, j , in a -0.5 to -0.9 V (vs. Ag/AgCl (sat. KCl)) potential window or diffusion limiting current density region of the CV recorded at 1600 rpm. However, $\alpha\text{-MnO}_2$ microspheres demonstrate a significant diffusion limiting current density of $-4.899 \text{ mA cm}^{-2}$, that is only slightly smaller than that of 20 wt.-% Pt@XC-72 ($-5.677 \text{ mA cm}^{-2}$), but significantly increased in comparison to Co_3O_4 nanoparticles ($j_L = -2.631 \text{ mA cm}^{-2}$) and 20 wt.-% Ir@XC-72 catalyst ($j_L = -3.974 \text{ mA cm}^{-2}$). The kinetic current densities calculated from the mass-transport correction of RDE at -0.2 V (vs. Ag/AgCl (sat. KCl)) show a trend similar to what is discernible for the diffusion limiting current densities: 20 wt.-% Pt@XC-72 ($11.909 \text{ mA cm}^{-2}$) > $\alpha\text{-MnO}_2$ microspheres (5.026 mA cm^{-2}) > Co_3O_4 nanoparticles (0.141 mA cm^{-2}) > 20 wt.-% Ir@XC-72 (0.109 mA cm^{-2}).

In order to study ORR kinetics and reduction pathways of the catalysts CVs at various rotational speeds were collected. A series of CVs of an $\alpha\text{-MnO}_2$ microspheres catalyst thin-film obtained at 400, 800, 1200 and 1600 rpm is presented in the inset of Figure 3b and shows an increase of well-defined diffusion limiting current density plateaus with increasing the rotational speed due to enhanced mass transfer to the electrode surface. Even more important, K-L plots at different potentials from the diffusion limiting region of the CVs were drawn in order to determine the number of electrons transferred during ORR. K-L plots obtained at -0.5 , -0.6 , -0.7 , -0.8 and -0.9 V (vs. Ag/AgCl (sat. KCl)) of an $\alpha\text{-MnO}_2$ microspheres catalyst thin-film are presented in Figure 3b and show very good linearity ($R^2 > 99.99\%$) indicating first order reaction kinetics with respect to dissolved O_2 .^[82] Moreover, near parallel K-L plots suggest potential independent electron transfer numbers within the examined potential range.^[83] Meanwhile, the number of electrons transferred, n_{e^-} , calculated from the K-L plots ranges from ~ 3.78 – 4.01 (average number of electrons transferred, $\bar{n}_{e^-} = 3.90$) and is fairly comparable to the commercial 20 wt.-% Pt@XC-72 catalyst ($n_{e^-} \approx 3.89$ – 4.03 , $\bar{n}_{e^-} = 3.99$) (Figure S4 and inset), suggesting a predominant direct four-electron reduction of O_2 to OH^- (Figure 3c). Although for Co_3O_4 and 20 wt.-% Ir@XC-72 a continuous increase in current density can be observed, no formation of plateau regions is found (Figure S5, S6 and insets). The calculated number of electrons transferred for Co_3O_4 and the commercial 20 wt.-% Ir@XC-72 catalyst is a mere ~ 2.25 – 2.93 ($\bar{n}_{e^-} = 2.79$) and ~ 3.40 – 3.52 ($\bar{n}_{e^-} = 3.47$), respectively, hence ORR must occur through a mixed form of a two- and four-electron transfer mechanism, which is likely to form hydroperoxyl radicals (HO_2^-) (see. Figure 3c).

Furthermore, Tafel analysis, which is commonly used to understand reaction mechanisms of electrocatalysts, was conducted.^[84] The slope obtained from the fit of the linear portion of the so-called Tafel plot to the Tafel equation expresses how much overvoltage increment is necessary to increase the current (density) by tenfold. Therefore, from a practical point of view, electrocatalysts should possess the smallest possible Tafel slope.^[85] Figure 3d shows representative Tafel plots of a thin-film of $\alpha\text{-MnO}_2$ microspheres, Co_3O_4 nanoparticles as well as commercial 20 wt.-% Pt@XC-72 and 20 wt.-% Ir@XC-72 catalyst obtained in the low current region of CVs within the ORR region. 20 wt.-% Pt@XC-72 exhibits the smallest Tafel slope of $\sim 62 \text{ mV dec}^{-1}$ and is in good agreement with Tafel slope values of Pt/C catalysts under alkaline conditions reported in the literature.^[86–89] Meanwhile, 20 wt.-% Ir@XC-72 and $\alpha\text{-MnO}_2$ microspheres possess the 2nd smallest Tafel slopes of approximately 85 mV dec^{-1} and 92 mV dec^{-1} underlining the satisfactory ORR kinetics and reaction rate, respectively. In comparison, Co_3O_4 nanoparticles exhibit the highest Tafel slope of 116 mV dec^{-1} indicating poor kinetics and reaction rate towards ORR.

The electrochemically active surface area (ECSA), which can be used as an indicator of catalytically active surface area and active site density as opposed to the mere BET surface area, was also determined. CVs of a $\alpha\text{-MnO}_2$ microspheres catalyst thin-film collected at different potential scan-rates in the non-Faradaic potential region are shown in Figure 3e. The CVs of $\alpha\text{-MnO}_2$ microspheres as well as the other catalysts investigated in this study show an almost rectangular shape (Figure 3e, S7 and S8), indicating electrochemical double-layer capacitive behaviour.^[90] Figure 3f shows the capacitive currents, \bar{I}_c , of $\alpha\text{-MnO}_2$ microspheres, Co_3O_4 nanoparticles and 20 wt.-% Pt@XC-72 as a function of the potential scan-rate as well as the linear fits to the data ($R^2 = 0.9764$ – 0.9995). Contrary to the assertion in the experimental section, $\alpha\text{-MnO}_2$ microspheres and Co_3O_4 nanoparticles do not show a straight line, but rather two slopes can be identified. This phenomenon, i.e. non-linear increase of double-layer capacitance with scan-rate, was first observed by Lodi and co-workers while studying porous RuO_2 -based film-electrodes in acid solution and further investigated in electrolytes with various pH.^[91] Recently, Li and co-workers found the same effect for mesoporous NiCo_2O_4 catalyst films in alkaline media.^[90] In contrast, Kolyagin and Kornienko, who investigated the wetting of porous hydrophobized gas diffusion electrodes, calculated the double-layer capacitance related to the total surface area wetted by electrolyte from the slopes of the tangents to the data obtained at low scan-rates leaving out the higher potential scan-rates where the plot deviates from linear behaviour.^[92] Other authors, in turn, simply assume a linear relationship and calculate the double-layer capacitance from the line of best fit.^[93–95] However, the authors ascribed deviation of specific capacitance from linearity with increasing potential scan-rate to be due to i) an easily accessible outer surface area, C_{outer} , that can be readily charged particularly at high potential scan-rates and ii) an inner surface area, C_{inner} , created by the pore network within the catalyst particle structure, which is less accessible due to mass transfer/diffusion limitation of ions

resulting in less charge stored and lower double-layer capacitance values, respectively.^[90,91,96] Therefore, capacitance at low potential scan-rates is representative of the total surface capacitance, i.e., the capacitance due to inner and outer surface area, whereas the capacitance at higher potential scan-rates corresponds to the charge of easily accessible outer surface area. Based on this assumption, the relationship $C_{\text{total}} = C_{\text{inner}} + C_{\text{outer}}$ can be established, which allows one to distinguish inner and outer ECSA of the catalysts.^[91,96] For the calculation of total ECSA, $ECSA_{\text{total}}$ capacitance values obtained at 0.005 to 0.05 V s^{-1} (1st slope) (Figure 3f) were used whereas the outer ECSA, $ECSA_{\text{outer}}$, was determined at scan-rates ranging from 0.05 to 0.4 V s^{-1} (2nd slope) (Figure 3f inset). Accordingly, the inner and outer ECSA of $\alpha\text{-MnO}_2$ microspheres was calculated to be 1.47 cm^2 and 0.87 cm^2 ($ECSA_{\text{total}} = 2.34 \text{ cm}^2$), respectively, indicating that nearly two thirds of the total ECSA arise from inner surface area. Co_3O_4 nanoparticles exhibit a total ECSA of 5.27 cm^2 including an inner and outer ECSA of 3.50 cm^2 and 1.76 cm^2 , respectively, which is more than twice that of $\alpha\text{-MnO}_2$ microspheres in terms of total ECSA. As it was believed that ECSA increases by increasing the amount of the particulate material and thus the total surface area within the thin-film, pure acetylene carbon black (AB) films with different mass loadings were probed with respect to their ECSA and the results are provided in the Supporting Information (Figure S9–S12). Although the results show a linear relationship for AB (Figure S13), they do not match the ECSAs associated with the BET specific surface areas of the corresponding metal oxide catalyst, indicating that either there is a discrepancy between both methods in general, or the surface area of $\alpha\text{-MnO}_2$ microspheres was not yet completely accessible to the electrolyte at the time of the measurement or is not accessible at all.^[97,98] On the contrary, the fit of commercial 20 wt.-% Pt@XC-72 displays only one slope, and the total ECSA can be calculated to be 5.60 cm^2 . While the contribution of AB's surface area ($s_{\text{BET}} = 95.1 \text{ m}^2 \text{ g}^{-1}$) to the total ECSA, which was originally added to ensure reasonably high electronic conductivity within the thin-films of $\alpha\text{-MnO}_2$ microspheres and Co_3O_4 nanoparticles, is assumed to be negligible ($ECSA_{\text{total}} = 0.47 \text{ cm}^2$), it can be adopted that a large portion of the 20 wt.-% Pt@XC-72 catalyst's ECSA arises from the surface area of Vulcan XC-72 carbon support ($s_{\text{BET}} = 300.4 \text{ m}^2 \text{ g}^{-1}$ from measurement of pure Vulcan XC-72). Note, since the double-layer capacitance from CVs at multiple scan-rates probes the entire surface including the carbon support, we would like to refer the reader to other techniques, for instance hydrogen underpotential deposition (H_{upd}) or CO-stripping voltammetry, being more accurate in assessing the ECSA of carbon supported precious metal catalysts.^[99]

Apart from the catalytic activity and ORR kinetics, the durability of the catalysts also plays a decisive role, especially when it comes to practical application. Durability towards ORR was evaluated by constant current chronopotentiometric stability measurements at a constant current density of -3 mA cm^{-2} in O_2 saturated 0.1 M KOH electrolyte at 1600 rpm and 25 °C. As can be seen in Figure 3g, the commercial 20 wt.-% Pt@XC-72 catalyst retained almost 99% of its initial overvoltage after 6 h and 12 h of continuous operation, respectively,

suggesting that no distinct degradation took place. Surprisingly, $\alpha\text{-MnO}_2$ microspheres at first show a decrease in overvoltage with time, reaching a maximum of $\sim 125\%$ after $\sim 2.35 \text{ h}$ ($\approx 141 \text{ min}$). Thereafter, the voltage slowly decays and finally comes to a $\sim 104\%$ after a total of 12 h of continuous constant current operation. This behaviour can be explained by the fact that the total surface area relevant to ORR catalysis is not instantly available due to a less accessible inner surface area within the $\alpha\text{-MnO}_2$ microspheres, that is likewise already recognized by the discrepancy between the BET specific surface area and ECSA, but will be steadily exposed during a certain break-in, e.g. conditioning period.

2.2.2. OER Activity and Stability Evaluation

Furthermore, the OER activity of the catalysts was investigated in O_2 -saturated 0.1 M KOH electrolyte at 1600 rpm and 10 mV s^{-1} potential scan-rate. Figure 4a shows representative CVs of the catalysts collected in a potential window of 0 to 0.9 V (vs. Ag/AgCl (sat. KCl)).

Two redox peaks can be identified within the CV of Co_3O_4 nanoparticles. The 1st peak at around 0.3 V (vs. Ag/AgCl (sat. KCl)) can be ascribed to the oxidation of Co^{2+} to Co^{3+} , while a 2nd peak located at $\sim 0.5 \text{ V}$ (vs. Ag/AgCl (sat. KCl)) corresponds to the oxidation of Co^{3+} to Co^{4+} .^[100] Meanwhile, Co_3O_4 reaches a current density of 10 mA cm^{-2} at a potential, $E_{j=10}$, of 0.610 V (vs. Ag/AgCl (sat. KCl)), which is significantly lower than the values of $\alpha\text{-MnO}_2$ microspheres ($E_{j=10} = 0.72 \text{ V}$) and 20 wt.-% Pt@XC-72 ($E_{j=10} = 0.84 \text{ V}$). Although a slightly lower potential of 0.60 V (vs. Ag/AgCl (sat. KCl)) could be found for the commercial 20 wt.-% Ir@XC-72 catalyst at 10 mA cm^{-2} , Co_3O_4 demonstrates a substantially stronger increase in current density with overvoltage, indicating its superior activity towards OER. It is worth mentioning that $\alpha\text{-MnO}_2$ microspheres likewise display sufficiently good OER activity, as their potential at 10 mA cm^{-2} is only $\sim 0.11 \text{ V}$ or $\sim 0.12 \text{ V}$ higher than that of Co_3O_4 or 20 wt.-% Ir@XC-72, respectively, but $\sim 0.12 \text{ V}$ lower as compared to 20 wt.-% Pt@XC-72.

To investigate the kinetics and reaction rate towards OER, Tafel plots of the catalyst thin-films were constructed from CVs in the low current region and the corresponding Tafel slopes of $\alpha\text{-MnO}_2$ microspheres, Co_3O_4 nanoparticles, commercial 20 wt.-% Pt@XC-72 and 20 wt.-% Ir@XC-72 are presented in Figure 4b. The lowest Tafel slope of 74 mV dec^{-1} could be observed for 20 wt.-% Ir@XC-72 catalyst, which is in good agreement with literature values found for Ir/C in 0.1 M KOH (60 mV dec^{-1}).^[101] Co_3O_4 nanoparticles exhibit the 2nd lowest Tafel slope of 128 mV dec^{-1} , but significantly smaller than that of $\alpha\text{-MnO}_2$ microspheres (226 mV dec^{-1}) and 20 wt.-% Pt@XC-72 (165 mV dec^{-1}), further confirming the good OER kinetics of Co_3O_4 nanoparticles.

To assess the durability of the catalysts towards the OER, constant current chronopotentiometric stability measurements in O_2 saturated 0.1 M KOH electrolyte at 1600 rpm and 25 °C were carried out. Figure 4c presents the potential response of a Co_3O_4 and a commercial 20 wt.-% Ir@XC-72 catalyst thin-film

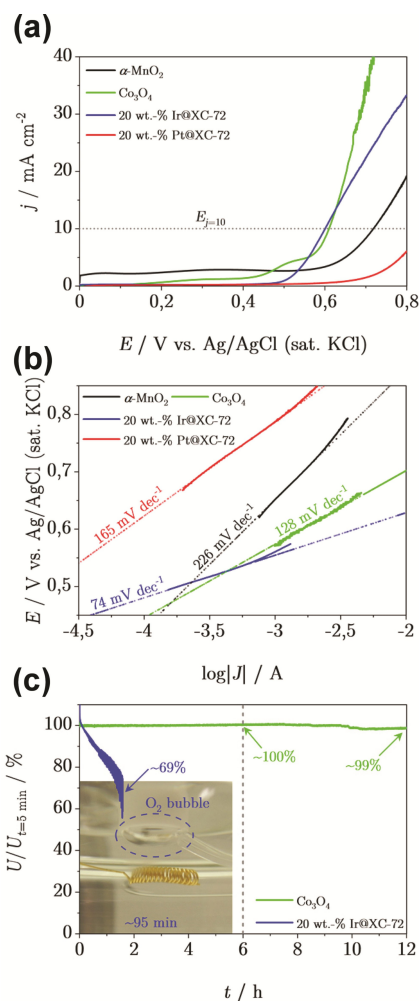


Figure 4. OER performance and stability evaluation. a) *iR*-corrected LSV curves of α - MnO_2 microspheres, Co_3O_4 nanoparticles, 20 wt.-% Ir@XC-72 and 20 wt.-% Pt@XC-72 in 25 °C equilibrated O_2 -saturated 0.1 M KOH at a potential scan-rate of 10 mV s^{-1} and rotational speed of 1600 rpm, b) Tafel plots (dashed lines) to the linear portion of the LSV curves in the low current region of the catalysts (solid lines), c) *iR*-corrected constant current chronopotentiometric response of Co_3O_4 nanoparticles and 20 wt.-% Ir@XC-72 in 25 °C equilibrated O_2 -saturated 0.1 M KOH at a rotational speed of 1600 rpm and constant current density operation of 10 mA cm^{-2} ; the inset shows a picture of a huge bubble formed on the 20 wt.-% Ir@XC-72 thin-film.

over a total of 12 h of constant current operation at 10 mA cm^{-2} . Co_3O_4 exhibits superior stability with almost 100% and 99% potential retention after 6 h and 12 h of operation, respectively. By contrast, the overvoltage of the 20 wt.-% Ir@XC-72 catalyst decreases sharply and is only ~69% of its initial value after about 2.35 h ($\hat{=}$ 141 min). As a large bubble could be observed on the 20 wt.-% Ir@XC-72 thin-film (Figure 4c inset), that obviously disturbed the stability measurement (fluctuating voltage profile), it was repeated at 2000 rpm (Figure S14). Although no obvious bubbles were present this time, the 20 wt.-% Ir@XC-72 thin-film began to peel off after approximately 4.4 h ($\hat{=}$ 264 min), indicating strong degradation of the catalyst as well as the carbon support under OER conditions. However, the results demonstrate the superior

electrochemical durability of Co_3O_4 over the commercial 20 wt.-% Ir@XC-72 catalyst in alkaline media.

2.3. Bifunctional α - MnO_2 and Co_3O_4 Catalysts

2.3.1. Physicochemical and Structural Characterization of the α - MnO_2 - Co_3O_4 Core-shell Catalyst

Figure 5a shows a SEM image of agglomerated α - MnO_2 - Co_3O_4 hybrid composite catalyst particles. On a higher magnification SEM image spherical structures characteristic of as-synthesized α - MnO_2 can be seen (Figure 5c and 5d), the average diameter of which is 3 to 4 μm (Figure 5b). Upon closer examination (Figure 5e), homogeneously distributed spherical Co_3O_4 particles with an average size of 25 to 30 nm can be recognized,

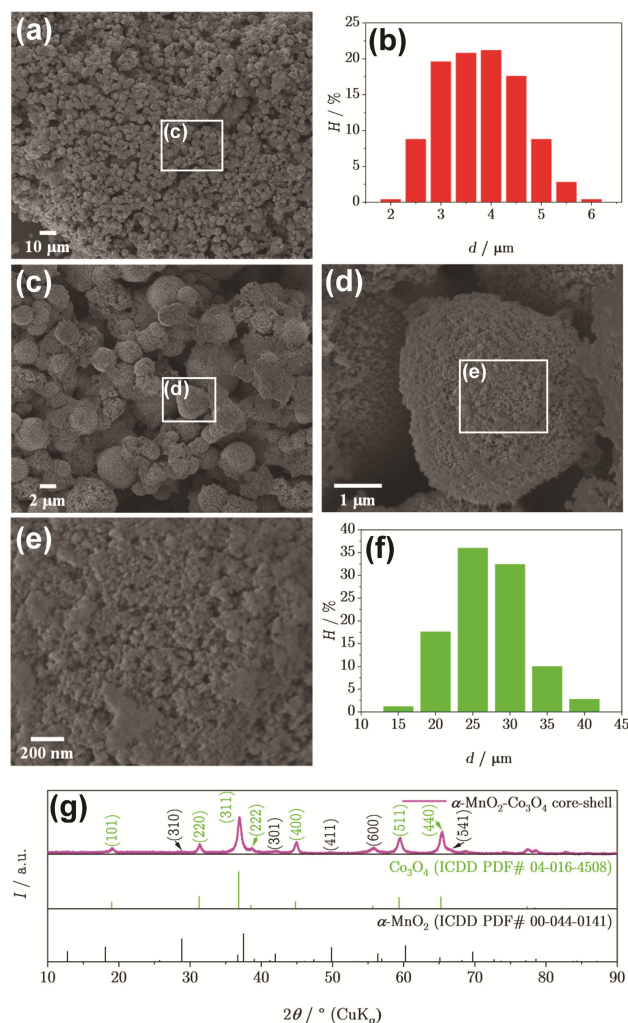


Figure 5. a) SEM image of agglomerated α - MnO_2 - Co_3O_4 core-shell particles, b) distribution of primary particle size based on evaluation of 250 particles, c) higher magnification SEM image of α - MnO_2 - Co_3O_4 core-shell particles, d) SEM image of a single α - MnO_2 - Co_3O_4 core-shell particle, e) SEM image of a α - MnO_2 - Co_3O_4 core-shell particle's surface at higher magnification, f) Size distribution of Co_3O_4 secondary particles occupying the shell based on evaluation of 250 nanoparticles, g) PXRD reflection pattern of as-synthesized α - MnO_2 - Co_3O_4 core-shell catalyst.

letting one draw the conclusion of Co_3O_4 nanoparticles grown on the surface of $\alpha\text{-MnO}_2$ microspheres merging into an $\alpha\text{-MnO}_2$ core Co_3O_4 shell structure. From the PXRD measurement, narrow and sharp reflections essentially originating from Co_3O_4 nanoparticles can be identified and features of $\alpha\text{-MnO}_2$ are hardly discernible, indicating a dense shell of Co_3O_4 nanoparticles around the $\alpha\text{-MnO}_2$ microspheres, that can be also confirmed by EDS results (Figure S15).

2.3.2. Bifunctional Activity and Stability Evaluation

Furthermore, electrochemical performance and stability of the $\alpha\text{-MnO}_2\text{-Co}_3\text{O}_4$ core-shell catalyst were evaluated. In addition, a thin-film containing a powder blend of $\alpha\text{-MnO}_2$ microspheres and Co_3O_4 nanoparticles with a 50:50 weight ratio was prepared and tested with regard to its bifunctional activity. As the hydrogen evolving reaction (HER) does not take place on $\alpha\text{-MnO}_2$ and Co_3O_4 , CVs were scanned in an extended potential window ranging from -1.3 to 1.1 V (vs. Ag/AgCl (sat. KCl)). Figure 6 presents the results of the performance and stability

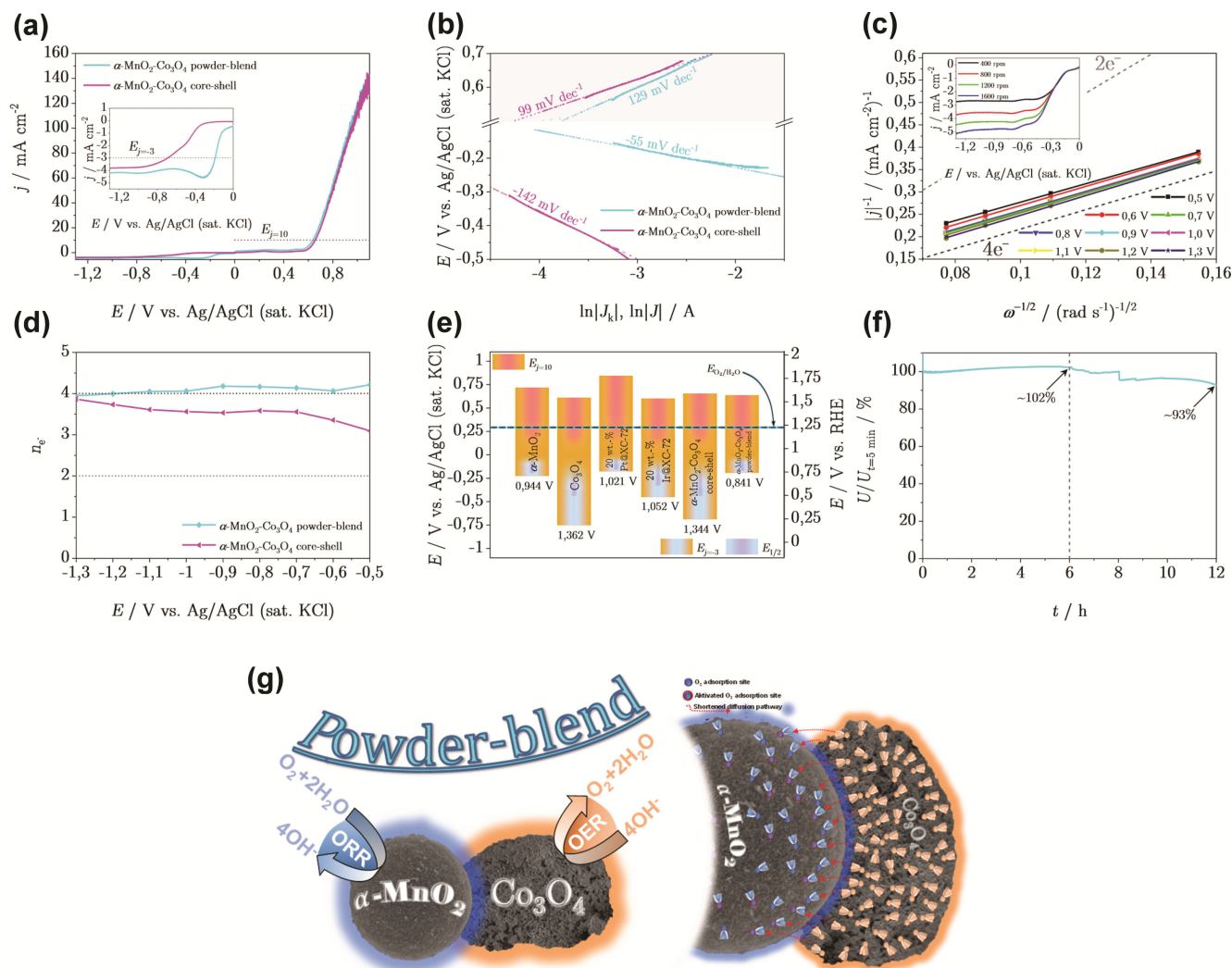


Figure 6. a) LSV curves of the $\alpha\text{-MnO}_2\text{-Co}_3\text{O}_4$ powder-blend and $\alpha\text{-MnO}_2\text{-Co}_3\text{O}_4$ core-shell catalyst in 25°C equilibrated O_2 -saturated 0.1 M KOH at a potential scan-rate of 10 mV s $^{-1}$ and 1600 rpm in an extended potential window within the ORR and OER region, ORR data (0 to -1.3 V (vs. Ag/AgCl (sat. KCl))) is iR - and bg -corrected, OER data (0 to 1.1 V (vs. Ag/AgCl (sat. KCl))) is iR -corrected. b) Tafel plots (dashed lines) to the linear portion of the LSV curves in the low current region of the ORR and OER (solid lines). c) K-L plots obtained at different potentials of the $\alpha\text{-MnO}_2\text{-Co}_3\text{O}_4$ powder-blend from iR - and bg -corrected LSV curves at various rotational speeds in 25°C equilibrated O_2 -saturated 0.1 M KOH at a potential scan-rate of 10 mV s $^{-1}$ (inset). d) Number of electrons transferred calculated from the K-L plots of the catalysts within a potential window of -0.5 to -1.3 V (vs. Ag/AgCl (sat. KCl)) of the $\alpha\text{-MnO}_2\text{-Co}_3\text{O}_4$ powder-blend and $\alpha\text{-MnO}_2\text{-Co}_3\text{O}_4$ core-shell catalyst. e) Final comparison of the catalysts investigated in this study by means of their potential difference, ΔE (orange bars), between $E_{j=-3}$ (blue bars) and $E_{j=10}$ (red bars) in the ORR and OER, respectively, the values below the bars represent the potential difference ($E_{1/2}$ was not used for the calculation of ΔE , but is inserted in the bars of $E_{j=-3}$ (purple bars) for comparison), the standard reduction potential for the $\text{O}_2/\text{H}_2\text{O}$ couple, $E_{\text{O}_2/\text{H}_2\text{O}} = 1.23$ V (vs. RHE) or 0.28 V (vs. Ag/AgCl (sat. KCl)), respectively, is highlighted (dashed line). f) iR -corrected constant current chronopotentiometric response of the $\alpha\text{-MnO}_2\text{-Co}_3\text{O}_4$ powder-blend in 25°C equilibrated O_2 -saturated 0.1 M KOH at a rotational speed of 1600 rpm and constant current density operation of 10 mA cm $^{-2}$. g) Schematic illustration of the proposed spill-over effect and shortened O_2 diffusion pathways within the $\alpha\text{-MnO}_2\text{-Co}_3\text{O}_4$ powder-blend.

evaluation of the α -MnO₂-Co₃O₄ powder-blend and α -MnO₂-Co₃O₄ core-shell catalyst. Figure 6a shows representative CVs of a thin-film containing the α -MnO₂-Co₃O₄ core-shell catalyst and α -MnO₂-Co₃O₄ powder-blend within the potential window of the ORR and OER in O₂ saturated 0.1 M KOH electrolyte at 1600 rpm and 10 mVs⁻¹ potential scan-rate. While the ORR performance of the α -MnO₂-Co₃O₄ core-shell catalyst ($E_{1/2} = -0.442$ V, $E_{j=-3} = -0.689$ V) could be slightly increased in comparison to a pure Co₃O₄ nanoparticles thin-film ($E_{1/2} = -0.647$ V, $E_{j=-3} = -0.894$ V), the powder-blend of both catalysts propels half-wave potential and potential at -3 mAcm⁻² to -0.172 V (vs. Ag/AgCl (sat. KCl)) and -0.193 V (vs. Ag/AgCl (sat. KCl)), respectively, which is now mere 11 mV or 16 mV higher than that of 20 wt.-% Pt@XC-72 in terms of $E_{1/2}$ and $E_{j=-3}$, respectively. In comparison, a pure α -MnO₂ microspheres thin-film exhibits marginally higher potentials of -0.197 V (vs. Ag/AgCl (sat. KCl)) and -0.226 V (vs. Ag/AgCl (sat. KCl)) regarding $E_{1/2}$ and $E_{j=-3}$, respectively. Similar results, i.e. increased performance when combining two highly active catalysts, have already been found in previous studies, in particular for the combination of Pt/C and Ba_{0.5}Sr_{0.5}Co_{0.8}O_{3- δ} ^[102], Pt and CaMnO₃^[103], Ag and Sm_{0.5}Sr_{0.5}CoO_{3- δ} ^[104] or Ag and Co₃O₄^[105]. Since an α -MnO₂-Co₃O₄ powder-blend sample with a 75:25 weight ratio also shows slightly increased activity towards ORR (Figure S16), a certain synergistic interaction at play between α -MnO₂ and Co₃O₄ can be considered. A possible synergy between these two catalysts could arise from a spill-over effect due to the presence of finely dispersed Co₃O₄ nanoparticles within the thin-film. This will promote the adsorption of O₂ on the α -MnO₂ microspheres surface as well as activate inert adsorption sites capable of accepting additional oxygen on the one hand, and providing an indirect pathway for subsequent reduction of O₂ formed on nanoparticulate Co₃O₄ due to the creation of shortened diffusion path lengths to the ORR catalytically active sites of α -MnO₂ microspheres on the other hand.^[106] A schematic illustration of the proposed synergistic mechanism between α -MnO₂ microspheres and Co₃O₄ nanoparticles is shown in Figure 6g. In contrast, the α -MnO₂-Co₃O₄ core-shell catalyst demonstrates poor activity particularly towards ORR, which is due to depletion of surface area and blocking of ORR catalytically active sites within the α -MnO₂ microspheres substrate structure by densely grown Co₃O₄ nanoparticles. Besides, the synergistic effect is also benefitting the overall kinetics and reaction rate. As can be seen in Figure 6b, Tafel analysis conducted in the low current region of representative CVs recorded on α -MnO₂-Co₃O₄ powder-blends reveal a significantly lower Tafel slope of ~ 55 mVdec⁻¹ towards ORR, which is even smaller than that of 20 wt.-% Pt@XC-72 (~ 60 mVdec⁻¹) and can be well ascribed to the enhanced O₂ adsorption capabilities of α -MnO₂ within the powder-blend, whereas the Tafel slope of Co₃O₄ nanoparticles during OER is still maintained. In order to find out to which extent electron reduction pathways are impacted by adding Co₃O₄ to α -MnO₂ microspheres, K-L plots from CVs at different rotational speeds were again drawn and the number of electrons transferred calculated. In the case of the α -MnO₂-Co₃O₄ core-shell catalyst a shift of the mixed kinetic-diffusion region to more negative potentials took place

(Figure S17). While the α -MnO₂-Co₃O₄ powder-blend still exhibits obvious diffusion limiting current density plateaus, they are only moderately developed for the α -MnO₂-Co₃O₄ core-shell catalyst. In the case of the α -MnO₂-Co₃O₄ powder-blend the number of electrons transferred calculated from the slopes of the K-L plots is 4.11 on average and yet still 3.94 at -1.3 V (vs. Ag/AgCl (sat. KCl)), implying that the direct four electron reduction pathway of α -MnO₂ microspheres is still maintained (Figure 6c and 6d). In comparison, the α -MnO₂-Co₃O₄ core-shell catalyst holds a number of electrons transferred of 3.55 on average, suggesting a mix of a 2 and 4 electron reduction pathway (Figure 6c and 6d). Furthermore, diffusion limiting current densities, j_L , and kinetic current densities, j_k , are calculated. The α -MnO₂-Co₃O₄ powder-blend exhibits a mean diffusion limiting current density of -4.09 mAcm⁻² being still in the range of pure α -MnO₂ microspheres (-4.899 mAcm⁻²), but significantly increased kinetic current density of 16.84 mAcm⁻² at -0.2 V (vs. Ag/AgCl (sat. KCl)) potential. In contrast, diffusion limiting current density and kinetic current density of the α -MnO₂-Co₃O₄ core-shell catalyst are calculated to be -3.35 mAcm⁻² and 0.096 mAcm⁻² at -0.2 V (vs. Ag/AgCl (sat. KCl)), respectively, which roughly corresponds to a mixed contribution of both catalysts. Meanwhile, the powder-blend reaches a current density of 10 mAcm⁻² at a potential of 0.637 V (vs. Ag/AgCl (sat. KCl)), which is only slightly higher than that of a pure Co₃O₄ ($E_{j=10} = 0.610$ V) as well as the commercial 20 wt.-% Ir@XC-72 ($E_{j=10} = 0.60$ V) thin-film, indicating that Co₃O₄ nanoparticles dominate the OER electrochemistry. The same applies to the α -MnO₂-Co₃O₄ core-shell catalyst needing a marginally higher potential of 0.655 V (vs. Ag/AgCl (sat. KCl)) to drive 10 mAcm⁻².

In order to evaluate the bifunctional activity of the catalysts, the potential difference, ΔE , between ORR and OER, i.e., the difference of potential needed to drive -3 mAcm⁻² ($E_{j=-3}$) and 10 mAcm⁻² ($E_{j=10}$), was also measured. Note, since voltage at a defined current density may represent the more practical comparative value, calculation of ΔE is based on $E_{j=-3}$ in lieu of half-wave potential, $E_{1/2}$, but is inserted (green bars) for comparison. As shown in Figure 6e, a simple α -MnO₂-Co₃O₄ powder-blend holds the smallest ΔE value of merely 0.841 V among the catalysts investigated in this study, demonstrating its superior bifunctional activity in alkaline electrolyte.

Since OER appears to be the more crucial oxygen reaction, stability of the α -MnO₂-Co₃O₄ powder blend was also tested by means of constant current chronopotentiometric stability measurements. After 12 h of constant current operation at 10 mAcm⁻² the powder-blend of α -MnO₂ microspheres and Co₃O₄ nanoparticles still demonstrates reasonably high voltage response of almost 93 % (Figure 6f).

3. Conclusions

In summary, high surface area α -MnO₂ microspheres in the form of 3D-hierarchically structured porous aggregates of cross-linked arbitrarily oriented needles and nanoparticulate Co₃O₄ were synthesized and their structural and physicochemical

properties related to catalytic performance parameters in KOH aqueous electrolyte evaluated using the Thin-film Rotating Disk Electrode technique. Both α -MnO₂ microspheres and Co₃O₄ nanoparticles exhibit superior ORR and OER activity, which is competitive to commercial Pt/C and Ir/C catalysts. In order to create a bifunctional catalyst, two approaches were pursued. First, Co₃O₄ nanoparticles were homogeneously grown on the surface of α -MnO₂ microspheres yielding a radial hybrid composite material in the form of a core (α -MnO₂) shell (Co₃O₄) structure, but demonstrated poor activity particularly towards ORR due to blocking of ORR catalytically active sites of α -MnO₂ by nanoparticulate Co₃O₄. In a second, much simpler, approach, individual α -MnO₂ microspheres and Co₃O₄ nanoparticles were physically mixed in a powder-blend demonstrating superior overall catalytic properties. It is observed that the individual catalysts still dominate their respective oxygen reaction and, in addition to that, synergistic interactions between both catalysts leading to slightly improved ORR kinetic activity could be achieved. The synergy between these two catalysts can be ascribed to a spill-over effect due to the presence of finely dispersed Co₃O₄ nanoparticles within the thin-film, which i) promote the adsorption of O₂ on the α -MnO₂ microspheres surface as well as activate inert adsorption sites capable of accepting additional oxygen, and ii) provide indirect pathways for subsequent reduction of O₂ formed on nanoparticulate Co₃O₄ due to the creation of shortened diffusion path lengths to the ORR catalytically active sites of α -MnO₂ microspheres. Mixing the individual catalysts indeed represents a very easy strategy to obtain bifunctionality, but offers considerable advantages when processing in gas diffusion electrodes, as properties such as the wetting behaviour of reactive layers comprising individual catalysts as well as their effect on the electrochemical performance can be tailored independently until finally combining the various materials in a customized bifunctional gas diffusion electrode.

Experimental Section

Materials

The materials in this work were used as received with specified purity grade: Manganese(II) sulphate monohydrate (MnSO₄·H₂O, ReagentPlus® grade, ≥ 99%), Potassium peroxodisulphate (K₂S₂O₈, ACS reagent grade, ≥ 99.0%), Potassium sulphate (K₂SO₄, Reagent-Plus® grade, ≥ 99.0%), Silver nitrate (AgNO₃, ACS reagent grade, ≥ 99.8%), 98% Sulphuric acid solution (H₂SO₄, EMSURE® grade), Tetrahydrofuran (THF, contains 250 ppm BHT as inhibitor, ACS reagent grade, ≥ 99.0%) and Potassium hydroxide (KOH, EMSURE® grade, > 85%) were purchased from Sigma Aldrich Chemie GmbH or Merck KGaA, respectively. Cobalt(II) acetate tetrahydrate (Co(CH₃COO)₂·4H₂O, > 99.0%) was received from Fluka AG. High-purity Potassium hydroxide (KOH, 99.98%) flakes were obtained from Carl Roth GmbH+Co. KG or Fisher Scientific GmbH, respectively. 95–97% Sulphuric acid solution was purchased from Bernd Kraft GmbH. 5 wt.-% LIQUIon™ Nafion™ solution (LQ-1005–000 EW) was received from Ion Power GmbH. Acetylene carbon black (AB, 42 nm average particle size, 99.99%) was obtained from Strem Chemicals Inc. 20 wt.-% Pt on Vulcan XC-72 (20 wt.-% Pt@XC-72, 2.0–3.0 nm metal particle size, 180–200 m²g⁻¹ total surface area) and 20 wt.-%

Ir on Vulcan XC-72 (20 wt.-% Ir@XC-72, 2.5–3.5 nm metal particle size, 180–200 m²g⁻¹ total surface area) were purchased from Premetek Co. Oxygen 5.0 (O₂, 99.999%) and Nitrogen 6.0 (N₂, 99.9999%) were provided by Rießner-Gase GmbH. All water used was double distilled water (dist. H₂O) produced from demineralized water using a distillation unit from Schott Geräte GmbH (~ 10 MΩ cm resistivity).

Synthesis of α -MnO₂ microspheres

As ORR catalyst α -MnO₂ microspheres were synthesized using a homogeneous one-step solution-based catalytic route as described earlier by Lin et al.^[66] with slight modifications. In brief, first 20 mmol (3.3803 g) of solid MnSO₄·H₂O, 20 mmol (5.4064 g) of solid K₂S₂O₈ and 20 mmol (3.4852 g) of solid K₂SO₄ were dissolved in 500 ml dist. H₂O one after each other under stirring at 650 rpm in an Erlenmeyer flask until a clear solution was formed, followed by dropwise addition of 20 ml 98% H₂SO₄ solution to adjust the pH level of the solution. After allowing it to cool down to room temperature again, 0.05 mmol (0.0849 g) solid AgNO₃ was added and further stirred for 15 min. Lastly 50 ml of the above solution were transferred into 10 beakers, covered with aluminium foil caps and heated in an oven (Mettmert GmbH+Co. KG, Schwabach, DE) at 40 °C for 8 h using 1 Kmin⁻¹ heating rate. After the oven has cooled down to room temperature the resulting black precipitates were collected and thoroughly washed several times with dist. H₂O using vacuum filtration until neutral pH and finally dried overnight (~ 16 h) at 80 °C in a preheated oven.

Synthesis of Co₃O₄ nanoparticles

As OER catalyst Co₃O₄ nanoparticles were synthesized using a hydrothermal synthesis route based on an approach described earlier by Dong et al.^[72] with some modifications. In a typical synthesis 1.3 g of solid Co(CH₃COO)₂·4H₂O were dissolved in 65 ml dist. H₂O under stirring at 700 rpm in a beaker for 5 min. Then 6.5 ml 25 wt.-% NH₃·H₂O solution were added dropwise to the clear solution under stirring at 700 rpm and subsequently stirred for a further 15 min until a viscous slurry had formed. Lastly 30 ml of the above slurry were transferred into an acid digestion vessel (Parr Instrument (Deutschland) GmbH, Frankfurt am Main, DE), sealed and heated in an oven (Mettmert GmbH+Co. KG, Schwabach, DE) at 100 °C for 3 h using 1 Kmin⁻¹ heating rate. After the vessel has cooled down to room temperature the black precipitates were collected and washed several times with dist. H₂O using centrifugation-redispersion at a rotational speed of 3500 rpm for 8 min until neutral pH and finally dried overnight (~ 16 h) at 80 °C in a preheated oven.

Preparation of α -MnO₂-Co₃O₄ core-shell structured catalyst

For the preparation of the core-shell structured composite catalyst comprising a 50:50 weight ratio of α -MnO₂ microspheres and Co₃O₄ nanoparticles, 0.15 g (overall yield of Co₃O₄ synthesis) of as-synthesized α -MnO₂ microspheres were first dispersed in 65 ml dist. H₂O, subsequently the hydrothermal synthesis of Co₃O₄ nanoparticles as described above was carried out, such that Co₃O₄ nanoparticles will be grown on the α -MnO₂ microspheres merging into a α -MnO₂ core Co₃O₄ shell structure. After heat treatment, the precipitates were collected and thoroughly washed several times with dist. H₂O using vacuum filtration until neutral pH and finally dried overnight (~ 16 h) at 80 °C in a preheated oven.

Structural and physicochemical characterisation

Phase composition and structural properties of the as-synthesized catalyst materials were examined by powder X-ray diffraction (PXRD) on a Philips X'Pert-MPD PW 3040/00 X-ray diffractometer (Malvern PANalytical B.V., formerly PANalytical B.V., Almelo, NL) in a Bragg-Brentano geometry with CuK_α radiation. PXRD data was recorded in a scanning range of 10° – 90° 2θ , step size of 0.01° 2θ and scanning speed of 0.8° 2θ s^{-1} . The evaluation of the PXRD data was conducted using X'Pert Highscore software. Particle size and morphological features were examined using a Zeiss/Leo Gemini 1530 high-resolution scanning electron microscope (SEM) equipped with a Schottky field emission gun (LEO Elektronenmikroskopie GmbH, Oberkochen, DE) at an acceleration voltage of 3 kV. For SEM analysis powder samples were sputter coated with a thin platinum layer (~ 1.3 nm) using a Cressington 208HR high resolution sputter coater (Cressington Scientific Instruments UK, Watford, England, UK). Elemental composition was determined by means of Energy dispersive X-ray spectroscopy (EDS) using a Link Pentafet 6498 EDS detector (Oxford instruments plc, Tubney Woods, Abingdon, UK) at an acceleration voltage of 15 kV, which was connected to a Jeol JSM-840 A Scanning electron microscope (Jeol (Germany) GmbH, Freising, DE) equipped with a LaB_6 cathode. For EDS analysis, powder samples were sputter coated with a thin carbon layer (~ 15 nm) using a Balzers SCD 004 sputter coater (Oerlikon Balzers Coating AG, formerly Balzers Union Limited, Balzers, LI). Inductively coupled plasma optical emission spectrometry (ICP-OES) was carried out on an Optima 7300 DV unit (PerkinElmer Inc., Waltham, Massachusetts, US) to probe the bulk elemental composition of the as-synthesized catalysts. Brunauer-Emmett-Teller (BET) specific surface area and pore size distribution measurements were performed by nitrogen adsorption-desorption at 77 K on a Micromeritics ASAP (Accelerated Surface Area and Porosimetry system) 2010 unit (Micromeritics Instrument Corp., Norcross, Georgia, US). Prior to measurements, catalyst powder samples were degassed for several hours at 80°C to remove adsorbed water and other surface contaminants. Pore size distribution was calculated by the Barrett-Joyner-Halenda (BJH) method from the desorption branch.

Catalyst activity and stability evaluation

Electrochemical measurements of the catalyst materials were carried out on a Thin-Film Rotating Disk Electrode (TF-RDE) setup with a three-electrode configuration connected to a computer controlled VMP3 Multi-channel potentiostat (Bio-Logic Science Instruments SAS, Seyssinet-Pariset, FR). E3 Series Fixed-Disk RDE-Tips (Pine Research Instrumentation Inc., North Carolina, Durham, US) with 5.0 mm diameter PTFE embedded Glassy Carbon (GC) disks mounted on a modulated speed rotator (Pine Research Instrumentation Inc., North Carolina, Durham, US), and 0.5 mm diameter gold wire coil (4x15 mm) (C3 Prozess- und Analysentechnik GmbH, Haar, DE) were used as working (WE) and counter electrode (CE), respectively. A double junction silver/silver chloride (Ag/AgCl) electrode (C3 Prozess- und Analysentechnik GmbH, Haar, DE) containing aqueous sat. KCl and 10% KNO_3 as inner and outer filling solutions served as reference electrode (RE). Data were acquired using Bio-Logic EC-Lab software.

GC disk working electrodes were first polished with a Buehler MasterPrep™ 0.05 μm Al_2O_3 polishing suspension on a Buehler PSA Microcloth in a "figure eight" pattern for 4 min to a mirror finish and then ultrasonicated in dist. H_2O and absolute ethanol. Afterwards the polished GC disk electrode was immersed to half its diameter in 3 M HClO_4 , dist. H_2O , 5 M KOH and dist. H_2O for 15 min each and again ultrasonicated in dist. H_2O and absolute ethanol. Finally, the GC disk electrode was mounted on an in-house built spin-coater for rotational drying at 700 rpm in air for at least 1 h.

Manganese oxide and cobalt oxide catalyst inks were prepared by mixing 0.05 g catalyst powder and 0.01 g acetylene carbon black (AB), followed by the addition of 10 ml Tetrahydrofuran (THF).^[107] Next, the catalyst ink was horn sonicated (Branson Ultrasonic SA, Urdorf, CH) for 20 s in a pulsed operation mode using a 1 s on/off interval duration and finally transferred to an ice water cooled ultrasonic bath for 1 h. 5 min prior to the ultrasonic treatment, 300 μl of a K^+ ion-exchanged Nafion® ionomer suspension (5 wt.-% LIQUion™ Nafion™ solution:0,1 M KOH \approx 2.2:1 weight ratio) was added to the ink. While it was still sonicated, a 10 μl aliquot of the well dispersed catalyst ink was pipetted with an Eppendorf pipette (Eppendorf AG, Hamburg, DE) onto the polished GC disk. Drying of the catalyst films was carried out by 15 min rotational drying in air on a spin-coater at 700 rpm immediately after drop casting, and 15 min stationary drying under an IR lamp in a beaker with presaturated THF atmosphere. Afterwards, it was allowed to cool down to room temperature for at least 1 h. Homogeneous smooth thin-film coatings on the GC disk could be achieved with a final composition of 250 $\mu\text{g}_{\text{catalyst}}\text{cm}^{-2}$, 50 $\mu\text{g}_{\text{AB}}\text{cm}^{-2}$ and 50 $\mu\text{g}_{\text{Nafion}^\circ}\text{cm}^{-2}$ per geometric area of GC disk electrode. Inks of commercial precious metal catalysts 20 wt.-% Pt@XC-72 and 20 wt.-% Ir@XC-72 were prepared using the same recipe, but without adding additional AB. Final composition was therefore 60 $\mu\text{g}_{\text{catalyst}}\text{cm}^{-2}$, 240 $\mu\text{g}_{\text{XC-72}}\text{cm}^{-2}$ and 50 $\mu\text{g}_{\text{Nafion}^\circ}\text{cm}^{-2}$ per geometric area of the GC disk electrode. Quality of the coating, particularly complete coverage of GC disk with catalyst film, was checked with a light microscope (Olympus K.K., Shinjuku, Tokio, JP).

All electrochemical measurements were performed in an in-house built glass cell consisting of an inner cell chamber with a total electrolyte volume of approximately 500 ml, and an integrated water jacket. The glassware was cleaned by soaking in 95–97% H_2SO_4 solution for 1 h and boiling twice in dist. H_2O for 1 h before every measurement.

Before the electrochemical measurements freshly prepared high-purity 0.1 KOH working electrolyte was saturated with O_2 by bubbling for 30 min as well as equilibrated to 25°C using an external heating circulator (Julabo GmbH, Seelbach, DE) connected to the water jacket of the glass cell. Then the coated GC disk WE was wetted with high-purity 0,1 M KOH and assembled together with the CE and RE/haber-luggin capillary. A gas-purged bearing assembly (Pine Research Instrumentation Inc., North Carolina, Durham, US) fitted on the shaft within the centre port of the glass cell was used to keep the inner cell chamber sealed to ambient air. During static measurements ($\omega=0$) the working electrolyte was blanketed with O_2 , while during rotation it was bubbled.

At first, conditioning of the coated GC disk WE was performed by running cyclic voltammograms (CVs) using a scan rate of 500 mV s^{-1} in a potential window of -1.15 to 0.95 V (vs. Ag/AgCl (sat. KCl)) at a rotational speed of 200 rpm, until the obtained CVs became stable.

Activity measurements were conducted by means of running two CVs with a scan rate of 10 mV s^{-1} in a potential window of -1.1 to 0.9 V (vs. Ag/AgCl (sat. KCl)) at a rotational speed of 1600 rpm. As comparative measures for the ORR and OER, potentials at -3 mA cm^{-2} , $E_{j=-3}$, and 10 mA cm^{-2} , $E_{j=10}$, per geometric area of the GC disk electrode were taken from the 2nd CV, respectively. The half-wave potential, $E_{1/2}$, was estimated by means of simplified derivative-extremum analysis and assigned to the potential in the local maximum of the dj/dE -curve.^[108–110] The potentials were referenced to the reversible hydrogen electrode (RHE) according to the conversion equation [Eq. (1)]:

$$E_{\text{RHE}} = E_{\text{Ag/AgCl (sat. KCl)}} + 0.059\text{ pH} + E_{\text{Ag/AgCl (sat. KCl)}}^0 \quad (1)$$

where E_{RHE} corresponds to the converted potential vs. RHE, $E_{\text{Ag/AgCl (sat. KCl)}}$ is the measured potential vs. Ag/AgCl (sat. KCl) and $E_{\text{Ag/AgCl (sat. KCl)} }^0$ represents the potential of Ag/AgCl (sat. KCl) vs. RHE (0.197 V).^[111] As $pH = 13$ (0.1 M KOH) is constant, the above equation can be simplified [Eq. (2)]:

$$E_{\text{RHE}} = E_{\text{Ag/AgCl (sat. KCl)}} + 0.946 \text{ V} \quad (2)$$

In order to determine the number of electrons, n_{e^-} , involved in the ORR, Koutecký-Levich (K-L) curves were developed based on Equations (3)–(6)

$$\frac{1}{j} = \frac{1}{j_k} + \frac{1}{j_L} \quad (3)$$

$$j_k = n_{e^-} F k C_{\text{O}_2} \quad (4)$$

$$j_L = B \omega^{-1} \quad (5)$$

$$B = 0.62 n_{e^-} F C_{\text{O}_2} D_{\text{O}_2}^{2/3} \nu^{<M>-1/6} \quad (6)$$

where j , j_k and j_L correspond to the measured, kinetic and diffusion limiting current density (mA cm^{-2}), respectively, F represents the Faraday constant (96485 C mol^{-1}), k the rate constant of the ORR (m s^{-1}), C_{O_2} is the saturated concentration of O_2 in 0.1 M KOH solution ($1.21 \cdot 10^{-6} \text{ mol cm}^{-3}$), B corresponds to the Levich constant, ω to the rotational speed of the GC disk WE (rad s^{-1}), n_{e^-} belongs to the overall number of e^- transferred during ORR, D_{O_2} is the diffusion coefficient of O_2 in 0.1 M KOH solution ($1.93 \cdot 10^{-5} \text{ cm}^2 \text{ s}^{-1}$) and ν is the kinematic viscosity of 0.1 M KOH solution ($0.0109 \text{ cm}^2 \text{ s}^{-1}$).^[112–114] The relevant CVs were collected in a potential window of 0 to -1.1 V (vs. Ag/AgCl (sat. KCl)) at rotational speeds of 400, 800, 1200 and 1600 rpm. Plotting the reciprocal absolute value of the measured current density, $|j|^{-1}$ ($\text{mA}^{-1} \text{ cm}^2$), at constant potentials of the diffusion limiting region vs. the reciprocal square root of the rotational speed, $\omega^{-0.5}$ ($(\text{rad s}^{-1})^{-0.5}$), and linear fitting gives K-L curves, whose slope complies with B and allows one to calculate the number of electrons transferred.^[83]

For Tafel analysis, the kinetic current, J_k (mA), was calculated from the mass-transport correction of CV data recorded in O_2 saturated electrolyte [Eq. (7)]:

$$J_k = \frac{J \times J_L}{J_L - J} \quad (7)$$

where J_k , J_L and J are the mass-transport corrected, diffusion limiting and measured current (mA), respectively.^[115] Tafel slopes were estimated by fitting the linear portion of the Tafel plot (natural logarithm of absolute kinetic current, $\ln |J_k|$, versus potential, E (vs. Ag/AgCl (sat. KCl))) in the low current region to the Tafel equation [Eq. (8)]:

$$E = a + b \ln J \quad (8)$$

with a slope, b , termed the Tafel slope and a constant, a , corresponding to the exchange current, J_0 .^[84]

Estimation of the Electrochemically Active Surface Area, ECSA, is based on measuring the capacitive current, I_c , related to the double-layer charging of CVs at multiple scan-rates (i.e. 0.005, 0.01, 0.025, 0.05, 0.1, 0.2 and 0.4 V s^{-1}) according to a previously published method.^[97,116,117] Therefore, CVs were collected in a 0.1 V potential window around the Open Circuit Potential, OCP, in the

non-Faradaic potential region. While I_c in OCP is in direct proportion to the product of the scan-rate, ν , and the electrochemical double-layer capacitance, C_{dl} , a plot of \bar{I}_c (mean value of absolute capacitive current taken from the anodic and cathodic sweep of the corresponding CV in the middle of the potential window, i.e., OCP) vs. ν gives a straight line whose slope corresponds to C_{dl} . Following the well-documented procedure in the literature^[97,116], ECSA is then the quotient of C_{dl} and specific capacitance, C_s [Eq. (9)]:

$$\text{ECSA} = \frac{C_{\text{dl}}}{C_s} \quad (9)$$

As C_s corresponds to the capacitance per geometric area of an atomically flat surface of the sample and is consequently difficult to determine, many authors tend to use values ranging from ~ 20 to $\sim 130 \mu\text{F cm}^{-2}$ considered general specific capacitances for a variety of catalyst materials.^[97,116,118–123] Since metal oxide surfaces differ a lot, taking general C_s values for the calculation of the ECSA is not universally applicable.^[123] Herein, the areal capacitance of a bare GC disk electrode ($C_s = 0.0709 \text{ mF cm}^{-2}$), which was determined under identical conditions as described above, was used to calculate the ECSA (Figure S1). In order to avoid interferences from the ORR, the related CVs were measured in N_2 saturated electrolyte.

Durability of the catalysts towards ORR and OER was evaluated by means of constant current chronopotentiometric stability measurements in O_2 saturated electrolyte at 1600 rpm at -3 mA cm^{-2} and 10 mA cm^{-2} constant current operation, respectively.

All data was corrected for capacitive background currents (bg correction) and ohmic potential drop (iR correction). To eliminate the contribution of capacitive background currents the measurement protocols including conditioning were repeated in N_2 saturated electrolyte and subtracted from the ORR scan profile. iR correction was done using the potentiostat's current interrupt technique at 80% compensation before starting a measurement protocol.

Acknowledgements

The financial support by the Federal Ministry of Research and Education (BMBF – Bundesministerium für Bildung und Forschung) within the InnoEMat project „PrintEnergy“ (grant no. 13XP5015F) is sincerely acknowledged. The authors would like to thank the project partners at Stuttgart Media University, VARTA Microbattery GmbH, Grillo-Werke AG, Elmeric GmbH and Etifix GmbH for the outstanding collaboration within this project. M.F.F. thanks the graduate school of the Bavarian Center for Battery Technology (BayBatt) for ongoing support. Furthermore, we would like to acknowledge Ingrid Otto and Birgit Brunner for the implementation of ICP-OES and BET measurements, respectively. M.F.F. gives his sincere thanks to Prof. Andreas Jess and Prof. Christina Roth who accepted him as a PhD student after Prof. Monika Willert-Porada departed this life in 2016. Open access funding enabled and organized by Projekt DEAL.

Conflict of Interest

The authors declare no conflict of interest.

Keywords: non-precious metal · bifunctional catalysts · manganese oxide · cobalt oxide · zinc-air batteries

- [1] J. Zhang, Q. Zhou, Y. Tang, L. Zhang, Y. Li, *Chem. Sci.* **2019**, *10*, 8924.
[2] V. Caramia, B. Bozzini, *Mater. Res.* **2014**, *3*.
[3] P. Gu, M. Zheng, Q. Zhao, X. Xiao, H. Xue, H. Pang, *J. Mater. Chem. A* **2017**, *5*, 7651.
[4] A. R. Mainar, E. Iruin, L. C. Colmenares, A. Kvasa, I. de Meaza, M. Bengoechea, O. Leonet, I. Boyano, Z. Zhang, J. A. Blazquez, *J. Energy Storage* **2018**, *15*, 304.
[5] Y. Li, M. Gong, Y. Liang, J. Feng, J.-E. Kim, H. Wang, G. Hong, B. Zhang, H. Dai, *Nat. Commun.* **2013**, *4*, 1805.
[6] S. Ren, X. Duan, S. Liang, M. Zhang, H. Zheng, *J. Mater. Chem. A* **2020**, *8*, 6144.
[7] E. Davari, D. G. Ivey, *Sustain. Energy Fuels* **2018**, *2*, 39.
[8] A. R. Mainar, L. C. Colmenares, O. Leonet, F. Alcaide, J. J. Iruin, S. Weinberger, V. Hacker, E. Iruin, I. Urdepilleta, J. A. Blazquez, *Electrochim. Acta* **2016**, *217*, 80.
[9] K. Selvakumar, S. M. Senthil Kumar, R. Thangamuthu, G. Kruthika, P. Murugan, *Int. J. Hydrogen Energy* **2014**, *39*, 21024.
[10] D. Yang, L. Zhang, X. Yan, X. Yao, *Small Methods* **2017**, *1*, 1700209.
[11] R. Cao, J.-S. Lee, M. Liu, J. Cho, *Adv. Energy Mater.* **2012**, *2*, 816.
[12] Y. Guo, Y.-N. Chen, H. Cui, Z. Zhou, *Chin. J. Catal.* **2019**, *40*, 1298.
[13] D. Chen, C. Chen, Z. M. Baiyee, Z. Shao, F. Ciucci, *Chem. Rev.* **2015**, *115*, 9869.
[14] X. Deng, H. Tüysüz, *ACS Catal.* **2014**, *4*, 3701.
[15] J.-S. Lee, S. Tai Kim, R. Cao, N.-S. Choi, M. Liu, K. T. Lee, J. Cho, *Adv. Energy Mater.* **2011**, *1*, 34.
[16] X. Cai, L. Lai, J. Lin, Z. Shen, *Mater. Horiz.* **2017**, *4*, 945.
[17] B. Lan, X. Zheng, G. Cheng, J. Han, W. Li, M. Sun, L. Yu, *Electrochim. Acta* **2018**, *283*, 459.
[18] Y. Ma, R. Wang, H. Wang, J. Key, S. Ji, *J. Power Sources* **2015**, *280*, 526.
[19] G. Cheng, S. Xie, B. Lan, X. Zheng, F. Ye, M. Sun, X. Lu, L. Yu, *J. Mater. Chem. A* **2016**, *4*, 16462.
[20] B. Zhang, G. Cheng, B. Lan, X. Zheng, M. Sun, F. Ye, L. Yu, X. Cheng, *CrystEngComm* **2016**, *18*, 6895.
[21] H. Antoni, D. M. Morales, J. Bitzer, Q. Fu, Y.-T. Chen, J. Masa, W. Kleist, W. Schuhmann, M. Muhler, *J. Catal.* **2019**, *374*, 335.
[22] Y. Meng, W. Song, H. Huang, Z. Ren, S.-Y. Chen, S. L. Suib, *J. Am. Chem. Soc.* **2014**, *136*, 11452.
[23] X. Zheng, L. Yu, B. Lan, G. Cheng, T. Lin, B. He, W. Ye, M. Sun, F. Ye, *J. Power Sources* **2017**, *362*, 332.
[24] K. Selvakumar, S. M. Senthil Kumar, R. Thangamuthu, K. Ganesan, P. Murugan, P. Rajput, S. N. Jha, D. Bhattacharyya, *J. Phys. Chem. C* **2015**, *119*, 6604.
[25] D. K. Walanda, G. A. Lawrance, S. W. Donne, *J. Power Sources* **2005**, *139*, 325.
[26] P. Ruetschi, *J. Electrochem. Soc.* **1984**, *131*, 2737.
[27] P. Ruetschi, R. Giovanoli, *J. Electrochem. Soc.* **1988**, *135*, 2663.
[28] J. Jia, P. Zhang, L. Chen, *Catal. Sci. Technol.* **2016**, *6*, 5841.
[29] J. Qi, W. Zhang, R. Cao, *ChemCatChem* **2018**, *10*, 1206.
[30] Z.-F. Huang, J. Wang, Y. Peng, C.-Y. Jung, A. Fisher, X. Wang, *Adv. Energy Mater.* **2017**, *7*, 1700544.
[31] P. W. Menezes, A. Indra, D. González-Flores, N. R. Sahraie, I. Zaharieva, M. Schwarze, P. Strasser, H. Dau, M. Driess, *ACS Catal.* **2015**, *5*, 2017.
[32] X. Lu, C. Zhao, *J. Mater. Chem. A* **2013**, *1*, 12053.
[33] Y. Xu, F. Zhang, T. Sheng, T. Ye, D. Yi, Y. Yang, S. Liu, X. Wang, J. Yao, *J. Mater. Chem. A* **2019**, *7*, 23191.
[34] M. S. Ahmed, B. Choi, Y.-B. Kim, *Sci. Rep.* **2018**, *8*, 2543.
[35] Y. Dou, T. Liao, Z. Ma, D. Tian, Q. Liu, F. Xiao, Z. Sun, J. Ho Kim, S. Xue Dou, *Nano Energy* **2016**, *30*, 267.
[36] B. Sidhureddy, J. S. Dondapati, A. Chen, *Chem. Commun. (Camb.)* **2019**, *55*, 3626.
[37] X. Li, F. Dong, N. Xu, T. Zhang, K. Li, J. Qiao, *ACS Appl. Mater. Interfaces* **2018**, *10*, 15591.
[38] G. Du, X. Liu, Y. Zong, T. S. A. Hor, A. Yu, Z. Liu, *Nanoscale* **2013**, *5*, 4657.
[39] X. Li, N. Xu, H. Li, M. Wang, L. Zhang, J. Qiao, *Green Energy Environ.* **2017**, *2*, 316.
[40] N. Xu, Y. Liu, X. Zhang, X. Li, A. Li, J. Qiao, J. Zhang, *Sci. Rep.* **2016**, *6*, 33590.
[41] M. J. Young, A. M. Holder, S. M. George, C. B. Musgrave, *Chem. Mater.* **2015**, *27*, 1172.
[42] C. K. King'odu, N. Opembe, C.-h. Chen, K. Ngala, H. Huang, A. Iyer, H. F. Garcés, S. L. Suib, *Adv. Funct. Mater.* **2011**, *21*, 312.
[43] C. M. Julien, A. Mauger, *Nanomaterials* **2017**, *7*.
[44] S. L. Suib, *J. Mater. Chem.* **2008**, *18*, 1623.
[45] T. Zhang, X. Zhang, J. Ng, H. Yang, J. Liu, D. D. Sun, *Chem. Commun. (Camb.)* **2011**, *47*, 1890.
[46] S. L. Suib, *Acc. Chem. Res.* **2008**, *41*, 479.
[47] M. Özacar, A. S. Poyraz, H. C. Genuino, C.-H. Kuo, Y. Meng, S. L. Suib, *Appl. Catal. A* **2013**, *462–463*, 64.
[48] J. E. Post, *Proc. Natl. Acad. Sci.* **1999**, *96*, 3447.
[49] A. S. Poyraz, J. Huang, C. J. Pelliccione, X. Tong, S. Cheng, L. Wu, Y. Zhu, A. C. Marschilok, K. J. Takeuchi, E. S. Takeuchi, *J. Mater. Chem. A* **2017**, *5*, 16914.
[50] R. D. Shannon, *Acta Crystallogr.* **1976**, *32*, 751.
[51] H. M. Abuzeid, A. M. Hashem, N. Narayanan, H. Ehrenberg, C. M. Julien, *Solid State Ionics* **2011**, *182*, 108.
[52] A. S. Poyraz, J. Huang, S. Cheng, L. Wu, X. Tong, Y. Zhu, A. C. Marschilok, K. J. Takeuchi, E. S. Takeuchi, *J. Electrochem. Soc.* **2017**, *164*, A1983-A1990.
[53] J. Huang, A. S. Poyraz, S.-Y. Lee, L. Wu, Y. Zhu, A. C. Marschilok, K. J. Takeuchi, E. S. Takeuchi, *ACS Appl. Mater. Interfaces* **2017**, *9*, 4333.
[54] J. Hou, Y. Li, L. Liu, L. Ren, X. Zhao, *J. Mater. Chem. A* **2013**, *1*, 6736.
[55] M. Thommes, K. Kaneko, A. V. Neimark, J. P. Olivier, F. Rodriguez-Reinoso, J. Rouquerol, K. S. W. Sing, *Pure Appl. Chem.* **2015**, *87*, 1051.
[56] E. Niwa, C. Uematsu, T. Hashimoto, *J. Am. Ceram. Soc.* **2012**, *95*, 3802.
[57] M. H. Alfaruqi, S. Islam, J. Gim, J. Song, S. Kim, D. T. Pham, J. Jo, Z. Xiu, V. Mathew, J. Kim, *Chem. Phys. Lett.* **2016**, *650*, 64.
[58] Y. Haoran, D. Lifang, L. Tao, C. Yong, *Sci. Works Higher Med. Inst.-Pleven* **2014**, *2014*, 791672.
[59] Y. J. Huang, W. S. Li, *J. Inorg. Mater.* **2013**, *28*, 341.
[60] K.-N. Jung, A. Riaz, S.-B. Lee, T.-H. Lim, S.-J. Park, R.-H. Song, S. Yoon, K.-H. Shin, J.-W. Lee, *J. Power Sources* **2013**, *244*, 328.
[61] L. Li, C. Nan, J. Lu, Q. Peng, Y. Li, *Chem. Commun. (Camb.)* **2012**, *48*, 6945.
[62] V. Subramanian, H. Zhu, R. Vajtai, P. M. Ajayan, B. Wei, *J. Phys. Chem. B* **2005**, *109*, 20207.
[63] V. B. R. Boppana, F. Jiao, *Chem. Commun. (Camb.)* **2011**, *47*, 8973.
[64] F. Cheng, Y. Su, J. Liang, Z. Tao, J. Chen, *Chem. Mater.* **2010**, *22*, 898.
[65] Y.-S. Ding, X.-f. Shen, S. Sithambaram, S. Gomez, R. Kumar, V. M. B. Crisostomo, S. L. Suib, M. Aindow, *Chem. Mater.* **2005**, *17*, 5382.
[66] T. Lin, L. Yu, M. Sun, G. Cheng, B. Lan, Z. Fu, *Chem. Eng. J.* **2016**, *286*, 114.
[67] W. Xiao, D. Wang, X. W. Lou, *J. Phys. Chem. C* **2010**, *114*, 1694.
[68] J. Zeng, J. R. Nair, C. Francia, S. Bodoardo, N. Penazzi, *Int. J. Electrochem. Sci.* **2013**, *8*, 3912.
[69] L. Zhang, C. Liu, L. Zhuang, W. Li, S. Zhou, J. Zhang, *Biosens. Bioelectron.* **2009**, *24*, 2825.
[70] M. Wang, W. Tan, X. Feng, L. K. Koopal, M. Liu, F. Liu, *Mater. Lett.* **2012**, *77*, 60.
[71] H. Yuan, L. Deng, Y. Qi, N. Kobayashi, M. Hasatani, *Int. J. Electrochem. Sci.* **2014**, *10*, 3693.
[72] Y. Dong, K. He, L. Yin, A. Zhang, *Nanotechnology* **2007**, *18*, 435602.
[73] X. Sun, R. You, X. Hu, J. Mo, R. Xiong, H. Ji, X. Li, S. Cai, C. Zheng, M. Meng, *RSC Adv.* **2015**, *5*, 35524.
[74] J. Rosen, G. S. Hutchings, F. Jiao, *J. Am. Chem. Soc.* **2013**, *135*, 4516.
[75] Q. Qu, J.-H. Zhang, J. Wang, Q.-Y. Li, C.-W. Xu, X. Lu, *Sci. Rep.* **2017**, *7*, 41542.
[76] S. Chen, Y. Zhao, B. Sun, Z. Ao, X. Xie, Y. Wei, G. Wang, *ACS Appl. Mater. Interfaces* **2015**, *7*, 3306.
[77] X. Zhang, J. Zhang, K. Wang, *ACS Appl. Mater. Interfaces* **2015**, *7*, 21745.
[78] C. Xiao, X. Lu, C. Zhao, *Chem. Commun. (Camb.)* **2014**, *50*, 10122.
[79] L. Xu, Q. Jiang, Z. Xiao, X. Li, J. Huo, S. Wang, L. Dai, *Angew. Chem. Int. Ed. Engl.* **2016**, *55*, 5277.
[80] B. You, N. Jiang, M. Sheng, M. W. Bhushan, Y. Sun, *ACS Catal.* **2016**, *6*, 714.
[81] D. E. Beltrán, S. Litster, *ACS Energy Lett.* **2019**, *4*, 1158.
[82] N. A. Anastasijević, V. Vesović, R. R. Adžić, *J. Electroanal. Chem. Interfacial Electrochem.* **1987**, *229*, 305.
[83] R. Zhou, Y. Zheng, M. Jaroniec, S.-Z. Qiao, *ACS Catal.* **2016**, *6*, 4720.
[84] T. Shinagawa, A. T. Garcia-Esparza, K. Takanebe, *Sci. Rep.* **2015**, *5*, 13801.
[85] M. Zeng, Y. Li, *J. Mater. Chem. A* **2015**, *3*, 14942.
[86] K. Tammeveski, M. Arulepp, T. Tenno, C. Ferrater, J. Claret, *Electrochim. Acta* **1997**, *42*, 2961.

- [87] S.-M. Park, S. Ho, S. Aruliah, M. F. Weber, C. A. Ward, R. D. Venter, S. Srinivasan, *J. Electrochem. Soc.* **1986**, *133*, 1641.
- [88] G. Couturier, D. W. Kirk, P. J. Hyde, S. Srinivasan, *Electrochim. Acta* **1987**, *32*, 995.
- [89] C. F. Zinola, A. M. Castro Luna, W. E. Triaca, A. J. Arvia, *J. Appl. Electrochem.* **1994**, *24*, 531.
- [90] G. Li, L. Anderson, Y. Chen, M. Pan, P. Y. Abel Chuang, *Sustain. Energy Fuels* **2018**, *2*, 237.
- [91] S. Ardizzzone, G. Fregonara, S. Trasatti, *Electrochim. Acta* **1990**, *35*, 263.
- [92] G. A. Kolyagin, V. L. Kornienko, *Russ. J. Appl. Chem.* **2007**, *80*, 1341.
- [93] F. Yang, S. Huang, B. Zhang, L. Hou, Y. Ding, W. Bao, C. Xu, W. Yang, Y. Li, *Nanomaterials* **2019**, *9*.
- [94] A. Tahira, Z. H. Ibupoto, R. Mazzaro, S. You, V. Morandi, M. M. Natile, M. Vagin, A. Vomiero, *ACS Appl. Mater. Interfaces* **2019**, *2*, 2053.
- [95] Y.-R. Hong, S. Mhin, K.-M. Kim, W.-S. Han, H. Choi, G. Ali, K. Y. Chung, H. J. Lee, S.-I. Moon, S. Dutta et al., *J. Mater. Chem. A* **2019**, *7*, 3592.
- [96] G. Lodi, E. Sivieri, A. de Battisti, S. Trasatti, *J. Appl. Electrochem.* **1978**, *8*, 135.
- [97] C. C. L. McCrory, S. Jung, I. M. Ferrer, S. M. Chatman, J. C. Peters, T. F. Jaramillo, *J. Am. Chem. Soc.* **2015**, *137*, 4347.
- [98] S. Jung, C. C. L. McCrory, I. M. Ferrer, J. C. Peters, T. F. Jaramillo, *J. Mater. Chem. A* **2016**, *4*, 3068.
- [99] S. Rudi, C. Cui, L. Gan, P. Strasser, *Electrocatalysis* **2014**, *5*, 408.
- [100] Z. Chen, C. X. Kronawitter, B. E. Koel, *Phys. Chem. Chem. Phys.* **2015**, *17*, 29387.
- [101] M. Gong, Y. Li, H. Wang, Y. Liang, J. Z. Wu, J. Zhou, J. Wang, T. Regier, F. Wei, H. Dai, *J. Am. Chem. Soc.* **2013**, *135*, 8452.
- [102] Y. Zhu, C. Su, X. Xu, W. Zhou, R. Ran, Z. Shao, *Chem. (Weinheim, Ger.)* **2014**, *20*, 15533.
- [103] X. Han, F. Cheng, T. Zhang, J. Yang, Y. Hu, J. Chen, *Adv. Mater.* **2014**, *26*, 2047.
- [104] Y. Zhang, Y. Guo, T. Liu, F. Feng, C. Wang, H. Hu, M. Wu, M. Ni, Z. Shao, *Front. Chem.* **2019**, *7*, 524.
- [105] H. M. A. Amin, C. J. Bondue, S. Eswara, U. Kaiser, H. Baltruschat, *Electrocatalysis* **2017**, *8*, 540.
- [106] W. C. Conner, J. L. Falconer, *Chem. Rev.* **1995**, *95*, 759.
- [107] J. Suntivich, H. A. Gasteiger, N. Yabuuchi, Y. Shao-Horn, *J. Electrochem. Soc.* **2010**, *157*, B1263.
- [108] F. Yin, Y. Liu, H. Liu, *J. Phys. Chem. C* **2020**, *124*, 1950.
- [109] E. M. Espinoza, J. A. Clark, J. Soliman, J. B. Derr, M. Morales, V. I. Vullev, *J. Electrochem. Soc.* **2019**, *166*, H3175-H3187.
- [110] A. Bonakdarpour, T. R. Dahn, R. T. Atanasoski, M. K. Debe, J. R. Dahn, *Electrochem. Solid-State Lett.* **2008**, *11*, B208.
- [111] A. J. Bard, L. R. Faulkner, *Electrochemical Methods: Fundam. Appl. Limnol.*, Wiley, Hoboken, Neth., **2001**.
- [112] X. Min, Y. Chen, M. W. Kanan, *Phys. Chem. Chem. Phys.* **2014**, *16*, 13601.
- [113] B. B. Blizanac, P. N. Ross, N. M. Marković, *J. Phys. Chem. B* **2006**, *110*, 4735.
- [114] P. Singh, D. A. Buttry, *J. Phys. Chem. C* **2012**, *116*, 10656.
- [115] Y. Zhang, T. Han, J. Fang, P. Xu, X. Li, J. Xu, C.-C. Liu, *J. Mater. Chem. A* **2014**, *2*, 11400.
- [116] C. C. L. McCrory, S. Jung, J. C. Peters, T. F. Jaramillo, *J. Am. Chem. Soc.* **2013**, *135*, 16977.
- [117] S. Trasatti, O. A. Petrii, *J. Electroanal. Chem.* **1992**, *327*, 353.
- [118] P. Connor, J. Schuch, B. Kaiser, W. Jaegermann, *Z. Phys. Chem.* **2020**, *234*, 979.
- [119] M. P. Browne, H. Nolan, G. S. Duesberg, P. E. Colavita, M. E. G. Lyons, *ACS Catal.* **2016**, *6*, 2408.
- [120] H. Han, Y.-R. Hong, J. Woo, S. Mhin, K. M. Kim, J. Kwon, H. Choi, Y.-C. Chung, T. Song, *Adv. Energy Mater.* **2019**, *9*, 1803799.
- [121] R. Boggio, A. Carugati, S. Trasatti, *J. Appl. Electrochem.* **1987**, *17*, 828.
- [122] M. J. Gira, K. P. Tkacz, J. R. Hampton, *Nano Convergence* **2016**, *3*, 6.
- [123] C. Wei, S. Sun, D. Mandler, X. Wang, S. Z. Qiao, Z. J. Xu, *Chem. Soc. Rev.* **2019**, *48*, 2518.

Manuscript received: October 14, 2020

Revised manuscript received: November 20, 2020

Accepted manuscript online: November 24, 2020